Atmos. Chem. Phys. Discuss., 10, 7265–7322, 2010
www.atmos-chem-phys-discuss.net/10/7265/2010/

Atmospheric Chemistry and Physics Discussions

This discussion paper is/has been under review for the journal Atmospheric Chemistry and Physics (ACP). Please refer to the corresponding final paper in ACP if available.

Observations of OH and HO_2 radicals over West Africa

R. Commane[1,*], C. F. A. Floquet[1,], T. Ingham[1,2], D. Stone[1,3], M. J. Evans[3], and D. E. Heard[1,2]**

[1]School of Chemistry, University of Leeds, Leeds, UK
[2]National Centre for Atmospheric Science, University of Leeds, Leeds, UK
[3]Institute for Climate And Atmospheric Science, School of Earth & Environment, University of Leeds, Leeds, UK
[*]now at: School of Engineering & Applied Sciences, Harvard University, Cambridge, USA
[**]now at: National Oceanography Centre, University of Southampton, Southampton, UK

Received: 11 February 2010 – Accepted: 11 March 2010 – Published: 18 March 2010

Correspondence to: D. E. Heard (d.e.heard@leeds.ac.uk)

Published by Copernicus Publications on behalf of the European Geosciences Union.

Abstract

The hydroxyl radical (OH) plays a key role in the oxidation of trace gases in the troposphere. However, observations of OH and the closely related hydroperoxy radical (HO_2) have been sparse, especially in the tropics. Based on a low-pressure laser-induced fluorescence technique (FAGE – Fluorescence Assay by Gas Expansion), an instrument has been developed to measure OH and HO_2 aboard the Facility for Airborne Atmospheric Measurement (FAAM) BAe-146 research aircraft. The instrument is described and the calibration method is discussed. During the African Monsoon Multidisciplinary Analyses (AMMA) campaign, observations of OH and HO_2 (HO_x) were made in the boundary layer and free troposphere over West Africa on 13 flights during July and August 2006. Mixing ratios of both OH and HO_2 were found to be highly variable but followed a diurnal cycle, with a median HO_2/OH ratio of 95. Daytime OH observations were compared with the primary production rate of OH from ozone photolysis in the presence of water vapour. Daytime HO_2 observations were generally reproduced by a simple steady-state HO_x calculation, where HO_x was assumed to be formed from the primary production of OH and lost through HO_2 self-reaction. Deviations between the observations and this simple model were found to be grouped into a number of specific cases: (a) in the presence of high levels of isoprene in the boundary layer, (b) within a biomass burning plume and (c) within cloud. In the forested boundary layer, HO_2 was underestimated at altitudes below 500 m but overestimated between 500 m and 2 km. In the biomass burning plume, OH and HO_2 were both significantly reduced compared to calculations. HO_2 was sampled in and around cloud, with significant short-lived reductions of HO_2 observed. HO_2 observations were better reproduced by a steady state calculation with heterogeneous loss of HO_2 onto cloud droplets included. Up to 9 pptv of HO_2 was observed at night, increasing early in the morning. Potential sources of high altitude HO_2 at night are also discussed.

ACPD

10, 7265–7322, 2010

1 Introduction

The concentration of the hydroxyl radical (OH) determines the daytime oxidative capacity of the atmosphere. Reaction with OH is the major removal pathway for trace gases such as methane (CH_4), carbon monoxide (CO), Volatile Organic Compounds (VOCs) and some halocarbons, often as the first and rate-determining step in their oxidation. A deeper knowledge of the distribution of the concentration of OH and HO_2 (collectively known as HO_x) helps our understanding of atmospheric oxidation and fast photochemical processes.

Usually the primary production pathway of OH in the troposphere, P(OH), is through the photolysis of ozone (O_3) and the subsequent reaction of $O(^1D)$ with water vapour (Ehhalt, 1999):

$$O_3 + h\nu(\lambda < 340\ \text{nm}) \longrightarrow O(^1D) + O_2 \quad \text{(R1)}$$

$$O(^1D) + H_2O \longrightarrow 2\ OH \quad \text{(R2)}$$

$$O(^1D) + M \longrightarrow O(^3P) + M \quad \text{(R3)}$$

The fraction of $O(^1D)$ reacting with water vapour to produce OH (F_{OH}) rather than being quenched to $O(^3P)$ (R3) depends on the water vapour concentration present and is 0.1–0.15 in typical boundary layer conditions. From this, the primary rate of OH production can then be calculated as:

$$P(OH) = 2\,J(O^1D)\,[O_3]\,F_{OH} \quad (1)$$

OH is quickly converted to the hydroperoxy radical (HO_2) by reaction with CO (Weinstock, 1969):

$$OH + CO \longrightarrow H + CO_2 \quad \text{(R4)}$$

$$H + O_2 \xrightarrow{M} HO_2 \quad \text{(R5)}$$

ACPD
10, 7265–7322, 2010

The reaction of OH with VOCs (Volatile Organic Compounds) produces peroxy radicals (RO_2), which, in the presence of NO (nitric oxide), leads to the formation of HO_2. NO is also important as it rapidly recycles HO_2 to form OH, allowing OH and HO_2 to be considered as a combined HO_x family. The ultimate fate of the HO_x radicals is to become a water soluble species such as H_2O_2 (through HO_2 self reaction) or HNO_3 (through the reaction of NO_2 with OH under high NO_x conditions), both of which can be wet or dry deposited.

Tropical regions with high levels of solar irradiation, and often high humidity, have the highest formation rates of OH (Bloss et al., 2005). The presence of high concentrations of OH and large surface areas allow tropical regions to dominate global oxidation of long-lived species. The rate of oxidation of CH_4 by OH is also highly dependent on temperature and 80% of this important climate gas is oxidised in the tropical troposphere (Bloss et al., 2005). The tropics also contain large regions of forest, which are a large source of global biogenic VOCs (Fehsenfeld et al., 1992; Guenther et al., 1995), with isoprene (C_5H_8) contributing about 40% of global VOC emissions (Guenther et al., 2006; Kesselmeier, 1999). Most biogenic emissions are controlled by solar irradiation and temperature (Kesselmeier, 1999; Fuentes et al., 2000). Global models calculate that over regions with high concentrations of biogenic VOCs, OH will be depleted compared to concentrations at similar latitudes (Poisson et al., 2000; von Kuhlmann et al., 2004; Lelieveld et al., 2002; Karl et al., 2007). However, while there have been some observations of HO_x in the mid-latitudes (e.g. Heard and Pilling, 2003, and references therein), observations in the tropics have been less extensive. In tropical marine air, OH mixing ratios up to 0.8 pptv and HO_2 mixing ratios between 2 and 45 pptv were observed during the PEM-Tropics-B (Tan et al., 2001) and INTEX-B (Mao et al., 2009) aircraft campaigns over the Pacific, while maximum OH and HO_2 mixing ratios of 0.37 pptv and 24 pptv respectively were observed at a surface site in the North Atlantic ocean (Whalley et al., 2009). However, Lelieveld et al. (2008) found that mixing ratios of OH and HO_2 observed in the presence of high concentrations of isoprene over the rainforests of Suriname were not depleted to the extent expected. OH mixing

ratios up to 0.8 pptv and HO_2 mixing ratios up to 80 pptv were observed (Martinez et al., 2008), much higher than calculated in modelling studies (Kubistin et al., 2008).

This paper presents airborne observations of OH and HO_2 radicals. The observations were made over tropical West Africa using a Fluorescence Assay by Gas Expansion (FAGE) instrument flown aboard the BAe-146 as part of the AMMA (African Monsoon Multidisciplinary Analyses) Special Observation Period 2 (SOP-2) intensive in July and August 2006. The instrument and the associated calibration procedure are described in some detail (Sect. 2). The radical concentrations reported from this instrument are presented in Sect. 3. The variation of HO_x with altitude is presented in Sect. 3.2 and is interpreted in terms of the changing chemical environment, detailed previously in Stewart et al. (2008), Capes et al. (2009) and Reeves et al. (2010). OH mixing ratios are compared to the primary production rate, while HO_2 mixing ratios are compared to a simple steady-state calculation. From these comparisons, a number of interesting cases were identified for further examination. These include observations of HO_x in the boundary layer over forested regions (Sect. 4.1), HO_x observations in a biomass burning plume (Sect. 4.2), HO_2 observed in and around cloud (Sect. 4.3) and HO_2 at night (Sect. 4.4). In an accompanying paper, Stone et al. (2010) compare the HO_x observations presented here with a comprehensive box model using the detailed Master Chemical Mechanism (MCM). A inter-comparison of HO_2 and peroxy radicals observed on two aircraft flying close together during AMMA is discussed in Andres-Hernandez et al. (2010).

2 Experimental

The Leeds Aircraft FAGE instrument was designed to be flown aboard the BAe-146 research aircraft operated by FAAM (Facility for Airborne Atmospheric Measurements). The instrument will be described in more detail in Ingham et al. (2010).

Fluorescence Assay by Gas Expansion (FAGE) is an on-resonance low pressure laser-induced fluorescence technique for the measurement of OH and HO_2 (Hard et al.,

1984). The strong $A^2\Sigma^+(v'=0) \leftarrow X^2\Pi_i(v''=0)$ $Q_1(2)$ transition of an OH molecule is excited by radiation at $\lambda \approx 308$ nm and the subsequent fluorescence is also detected at $\lambda \approx 308$ nm. The fluorescence cell is maintained at low pressure (ranging from 1.5 Torr at 9 km to 2.5 Torr at sea level) to ensure the fluorescence from the OH molecule lasts longer than the laser excitation pulse, which allows for temporal gating of the fluorescence detection. OH and HO_2 are detected simultaneously with two excitation axes in series. After the OH detection axis, NO is added to the air flow to titrate HO_2 in the sample gas to OH, which is detected in the HO_2 axis.

$$HO_2 + NO \longrightarrow OH + NO_2 \quad \text{(R6)}$$

The sensitivity of the instrument to OH and HO_2 must be determined by calibration. Figure 1 shows the instrument set-up. The instrumentation is installed on two 19 inch aircraft racks, located behind the fluorescence cell sampling point with pumps located below the fluorescence cell.

2.1 HO_x radical sampling

Ambient air from outside the aircraft is sampled through an inlet (adapted from Eisele et al., 1997) mounted on a window blank on the starboard side of the BAe-146, close to the front of the aircraft. Using two concentric tubes with restrictions, the inlet slows the air prior to sampling, while minimising turbulence, and hence wall contact, and the associated loss of OH radicals.

Air is drawn in through a pinhole (0.75 mm diameter) to a fluorescence cell maintained at reduced pressure by a rotary pump (Leybold Trivac D25B) coupled with a supercharger (Eaton M90). In order to extend outside the aircraft skin and deliver OH to the excitation axis, a tube made of anodised aluminium (internal diameter = 5 cm; length = 50 cm) was added to the fluorescence cell. Characterisation tests on the cell (Ingham et al., 2010) have shown significant OH loss on contact with the internal tube walls, thus reducing the instrument sensitivity to OH. No solar scattered light has been detected at either the OH or HO_2 detection axes when the instrument was operated on

the aircraft. A fluorescence cell for the detection of RO_2 is shown in Fig. 1 but is not yet operational.

2.2 Laser excitation of OH

Laser light at $\lambda \approx 308$ nm was generated by a laser system consisting of a Nd:YAG (Neodymium-ion doped Yttrium Aluminium Garnet ($Y_3Al_5O_{12}$) DS20-532, Photonics Industries) pumped Titanium Sapphire (Ti:Sapp) laser (TU-UV 308 nm, Photonics Industries). The YAG laser typically produces 9–10 W of light at λ=532 nm and a Pulse Repetition Frequency (PRF) of 5 kHz, which is used to pump the Ti:Sapp laser. The Ti:Sapp output wavelength of $\lambda \approx 924$ nm is selected through the use of a diffraction grating and is passed through the first of two non-linear harmonic generation stages consisting of a Cerium Lithium Borate (CLBO) crystal, generating the second harmonic at $\lambda \approx 462$ nm. A half wave plate corrects the polarisation of the light to allow the second crystal to perform sum-frequency mixing of the second harmonic ($\lambda \approx 462$ nm) with the fundamental ($\lambda \approx 924$ nm), producing light at $\lambda \approx 308$ nm.

Under optimal conditions, ~100 mW of UV radiation is produced with a pulse width of 35 ns (Full Width Half Maximum, FWHM) and a laser linewidth of 0.065 cm^{-1}. However, during the observations presented here, typical powers observed after adjustment varied from 30 mW to 50 mW at $\lambda \approx 308$ nm. Dielectric coated beam splitting mirrors split the UV beam before launching the light into fibre optic cables (Oz Optics) in the ratio 60%:36%:4% for use within the OH and HO_2 axes and the reference cell respectively. Upon exiting the fibre optic cable, the laser beam entering each detection cell is collimated and baffled before intersecting the air sample. After traversing the excitation region, the beam exits the cell through another baffled arm and is directed (via a 45° mirror) into a calibrated UV photodiode (UDT – 555UV, Optoelectronics), allowing real-time measurement of the laser power. The measured laser power is used to normalise the fluorescence signal for fluctuations in laser power.

2.3 Fluorescence detection

In the fluorescence cell (Fig. 2), the UV fluorescence is collected and passed through an interference filter (Barr Associates ∼50% transmission at λ=308 nm, FWHM ca. 5 nm centered at λ=308 nm). A back reflecting mirror (CVI Optics) improves the signal collection efficiency. The fluorescence signal is then focused onto the Channel Photomultiplier (CPM) (Perkin-Elmer 943P, $\sim 5 \times 10^8$ gain), where the electron pulses generated from a single photon are counted with a photon-counting card (PMS 400, Becker and Hickl). To prevent saturation, the CPM is turned off by a high voltage switching circuit ("gating box", designed and built in-house) from the time the laser is triggered until ∼60 ns after the laser pulse (FWHM=35 ns). The use of a temporal gating allows sensitive measurement of the fluorescence emitted from the electronically excited OH and discrimination against laser scattered light.

2.4 Reference cell

The wavelength of the laser is changed by a stepper motor which controls the angle of the diffraction grating within the Ti:Sapp laser cavity. The absolute wavelength of the second harmonic of the Ti: Sapp ($\lambda \approx 462$ nm) is monitored by a wavemeter (Wavemaster 33–2650, Coherent). However, the resolution of this wavemeter (precision ±0.001 nm, accuracy ±0.005 nm) is insufficient to locate the OH $Q_1(2)$ rotational line (λ=307.995 nm). The reference cell facilitates scanning over and identification of the $Q_1(2)$ peak. With the reference cell maintained at low pressure (∼3 Torr), humidified cabin air is passed over an electrically heated 80:20 Ni:Chrome filament, producing OH radicals by pyrolysis of water vapour (Stevens et al., 1994; Wennberg et al., 1994). The reference cell receives 2–3 mW (∼4%) of the total UV radiation. The OH fluorescence signal is filtered and focussed on to a CPM perpendicular to the laser beam. The resulting signal is recorded using a photon-counting card. Because of the high concentration of OH radicals produced in the reference cell, discriminating the OH

fluorescence signal from the background laser scatter does not require gating of the CPM.

Figure 3 shows the signal observed in the reference cell for a two minute measurement cycle. The OH signal in the reference cell is typically 20 000 cts s^{-1} above the laser scatter background of approximately 7000 cts s^{-1}. The first 55 points on the figure show the OH fluorescence while scanning over the $Q_1(2)$ rotational line of OH to locate the wavelength of the peak fluorescence (*finding line*: from λ=307.990 nm to λ=308.000 nm). Points ~55–175 show the *online* fluorescence signal (and background) as the laser wavelength is tuned to the peak of fluorescence. Points ~175–235 show the fluorescence as the laser wavelength is tuned to a wavelength which does not induce fluorescence to measure the background signal (*offline*).

The signal in the reference cell varies with aircraft cabin pressure due to changes in the laser wavelength. The variation in the wavelength generated by the laser is due to the changing refractive index of the cabin air with pressure compared with the material of the laser grating. This change in wavelength away from the maximum of the OH transition results in the signal due to OH fluorescence varying with cabin pressure. Independent of this laser wavelength change with pressure, fluctuations in cell pressure will also alter the instrument sensitivity. While the effect of changing cell pressure on sensitivity can be determined by calibration, it cannot be decoupled from changes in wavelength during AMMA as the Ti:Sapp laser cavity was not kept at constant pressure, so only data recorded on level flights (with constant laser wavelength) are considered.

2.5 Data analysis

The laser is operated at a pulse repetition frequency of 5 kHz and the contribution of the solar and dark counts (CPM thermal noise) to the observed signal is determined for each laser pulse. The fluorescence signal is collected for 1 µs (Gate A). After a 5 µs gap the non-laser background signal is recorded for 20 µs (Gate B) and the signal

solely due to OH fluorescence and laser background, Sig_{fl}, is calculated:

$$Sig_{fl} = SigA - \frac{SigB}{20}, \quad (2)$$

where SigA (cts) is the number of counts in the 1 µs collection Gate A (cts s^{-1}) and SigB/20 is the number of counts in the 20 µs collection gate (typically 0–1 cts s^{-1}). The total signal, Sig_{fl} (cts s^{-1}), is then recorded at 1 Hz and normalised for laser power (P, mW). For OH, the normalised offline signal OH $Sig_{offline}$ is subtracted from the normalised online signal OH Sig_{online}, leaving the signal solely due to OH (OH Sig, cts s^{-1} mW^{-1}):

$$OHSig = OHSig_{online} - OHSig_{offline} \quad (3)$$

HO_2Sig is the difference in normalised online signal observed with NO injected (HO_2+OH) and without NO added (OH only). The concentration of OH is then calculated using the experimentally determined instrument sensitivity (C_{OH}, cts s^{-1} mW^{-1} molecule^{-1} cm^3):

$$[OH] = \frac{OHSig}{C_{OH}} \quad (4)$$

The concentration of HO_2 is calculated using the experimentally determined instrument sensitivity HO_2 (C_{HO_2}, cts s^{-1} mW^{-1} molecule^{-1} cm^3):

$$[HO_2] = \frac{HO_2Sig}{C_{HO_2}} \quad (5)$$

2.6 Calibration

Before and after deployment, the instrument sensitivity was determined over the range of cell pressures experienced during the AMMA campaign (between 1.5 and 2.1 Torr, equivalent to 2–2.8 hPa) using a method similar to that employed by Faloona et al.

(2004) and Martinez et al. (2008). Pinholes with diameters between 0.65 and 0.85 mm were used to obtain cell pressures between 1.5 and 2.7 Torr (2–3.6 hPa) respectively.

By varying the lamp current supplied to a low-pressure mercury lamp, a range of concentrations of OH and HO_2 were produced from the photolysis of humidified air (constant $[H_2O]$) at $\lambda \approx 184.9$ nm:

$$[OH] = [HO_2] = [H_2O]\ \sigma_{H_2O}\ \phi_{OH}\ F\ \delta t \quad (6)$$

where σ_{H_2O} is the absorption cross-section of water at λ=184.9 nm ($7.14 \pm 0.2 \times 10^{-20}$ molecule^{-1} cm^2; Cantrell et al., 1997a), ϕ_{OH} and ϕ_{HO_2} are the photodissociation quantum yields of OH and HO_2 respectively (=1), F is the photon flux of the mercury lamp (photon cm^{-2} s^{-1}) at λ=184.9 nm and δt is the residence time in the photolysis region.

Figure 4 shows the experimental set-up of the calibration system. A known flow (ca. 50 slm: L min^{-1} at standard temperature and pressure) of ultra high-purity air (BTCA 178, BOC Special Gases) is introduced into the system, with a variable fraction of the flow diverted (through bypass valves) to a bubbler containing distilled water in order to humidify the air. After mixing, most of the calibration gas passes through a 1.27 cm × 1.27 cm black-anodised square aluminium tube 30 cm long, where the gas is photolysed by the λ=184.9 nm emission of a mercury lamp of known actinic flux (see below) to produce equal concentrations of OH and HO_2 before delivery to the FAGE sampling point. Immediately prior to the air entering the calibration tube, a small flow is diverted to a dew-point hygrometer (CR4, Buck Research Instruments) to measure the concentration of water vapour in the flow. There are three 3.81 cm Suprasil® windows separated by equal distance down the length of the calibration tube. At high flow rates through the calibration tube, the gas was found to have a uniform velocity profile consistent with turbulent flow. The mercury lamp is housed in a nitrogen-purged aluminium casing, and usually mounted over the window closest to the exit of the calibration tube. This purged housing is heated to maintain a stable lamp temperature (±1 °C), while the nitrogen flow prevents both ozone formation within the housing and absorption of radiation by ambient water vapour and oxygen prior to the light entering the calibration

tube. The lamp is collimated using thin walled tubes (3 mm diameter, 8 mm length) packed together in front of the lamp. These tubes are used to create a more uniform actinic flux in the photolysis region.

Prior to calibration, the lamp flux at λ=184.9 nm was determined by N_2O actinometry through the generation of a quantifiable mixing ratio of NO from the photolysis of 10% N_2O in air. The theory and method of this technique has been described extensively in previous publications (e.g. Edwards et al., 2003; Faloona et al., 2004; Glowacki et al., 2007; Whalley et al., 2007). Two corrections were made in the calculation of the flux, F. In the NO_x analyser (Thermo Electro 42C; detection limit/precision ~50 pptv) used to measure the NO produced, the introduction of high concentrations of N_2O results in the reporting of artificially low NO mixing ratios. This is due to increased quenching of the electronically excited NO_2 fluorescence by N_2O within the analyser. The effect of this quenching was characterised and the corrected NO mixing ratios were calculated. The second correction accounted for absorption of the light flux by N_2O across the width of the photolysis area (Edwards et al., 2003). A linear relationship between the lamp current supplied to the lamp and the flux was observed after corrections, allowing the lamp current to be varied to generate various concentrations of HO_x.

Calibrations were conducted over a range of water vapour mixing ratios from 330 ppmv to 10 000 ppmv. Figure 5 shows a typical multi-point calibration for the lowest water vapour used (332 ppmv). The instrument sensitivity to OH is a function of water vapour in the gas flow (Smith et al., 2006) due to quenching of electronically excited OH by the water vapour. Using a constant concentration of water vapour during calibrations ensures a linear relationship between the observed signal and concentration of OH or HO_2.

Over the pressure range observed in the fluorescence cell during AMMA, the sensitivity of the instrument did not vary significantly (Fig. 6) and the mean sensitivities of the instrument to OH (C_{OH}=6.29 (±0.95) $\times 10^{-8}$ cts s^{-1} mW^{-1} $molecule^{-1}$ cm^3, $\pm 1\sigma$ standard deviation) and HO_2 (C_{HO_2}=1.17 (±0.23)$\times 10^{-7}$ cts s^{-1} mW^{-1} $molecule^{-1}$ cm^3) were determined. Calibrations before and after the campaign did not show any

degradation in the instrument sensitivity, and while in-flight calibrations were not possible during the AMMA campaign, instrumentation to allow calibration during flight is currently being developed. The instrument sensitivity to OH is half that of HO_2 and is due to a higher loss of OH compared to HO_2 on the surface of the cell between sampling and detection.

2.7 Limit of detection

It is possible to calculate the instrumental Limit Of Detection (LOD) for OH and HO_2 by carrying out a t-test between an observations value and zero (0 molecule cm^{-3}), assuming the variance in the background is constant throughout the measurement cycle and is represented by the variance in the offline measurement. For unequal sample sizes (online and offline), the minimum detectable HO_x, Sig_{min}, for a given confidence interval can be calculated:

$$Sig_{min} = T_{CI} \sqrt{\frac{1}{n} + \frac{1}{m}}\, \sigma_{bg} \tag{7}$$

where T_{CI} is the T value for a given confidence interval ($T_{69\%}$=1), n and m are the sample sizes online and offline respectively defined by the sampling frequency and σ_{bg} is the standard deviation of the background, which is assumed to be representative of the standard deviation of the background signal during the online sample. Previous studies have assumed the background signal obeys Poisson statistics (Stevens et al., 1994; Faloona et al., 2004; Martinez et al., 2008) and:

$$\sigma_{bg} = \sqrt{(S_{lb} + S_{sb} + S_{dc})} \tag{8}$$

where S_{lb} is the signal due to laser scatter, S_{sb} is the signal due to solar background and S_{dc} are the dark counts of the CPM.

Sig_{min} is converted into a minimum detectable concentration of OH (and HO_2) by:

$$[OH_{min}] = \frac{OHSig_{min}}{C_{OH}\, P} \tag{9}$$

$$[HO_{2\ min}] = \frac{HO_2 Sig_{min}}{C_{HO_2}\ P} \quad (10)$$

where C_{OH} and C_{HO_2} are the instrument sensitivity to OH and HO_x (cts s^{-1} mW^{-1} $molecule^{-1}$ cm^3) respectively and P is the laser power in the cell (mW).

Using a confidence interval of 69% (T value =1), a limit of detection is calculated for each measurement cycle (~5 min). Table 1 shows the OH and HO_2 LODs calculated for a typical measurement cycle during the AMMA aircraft campaign (July–August 2006). During the campaign the mean OH LOD was 7.1×10^5 molecule cm^{-3} and the mean HO_2 LOD was 7.5×10^5 molecule cm^{-3} for a one minute integration time. In order to improve sensitivity to HO_2, the time between laser trigger and fluorescence collection is shortened, compared to that set for OH, which increases the background signal (and therefore σ_{bg}) and hence limit of detection but will also increase the sensitivity to HO_2. This shortened delay time is suitable for HO_2 observations, as a typical concentration of HO_2 in the atmosphere is around two orders of magnitude greater than the calculated LOD.

During AMMA, the performance of the YAG laser was degraded during flight in line with an increase in cabin temperature, which often increased from 15 °C to 35 °C during a flight. The reduced power output from the YAG resulted in the Ti:Sapphire laser taking longer to reach the lasing threshold. The time delay between the laser trigger and the laser pulse was found to increase by several tens of nanoseconds during a given flight, an increase large enough to increase the laser background signal and affect both the sensitivity of the instrument to HO_x and the instrumental limit of detection. As the background is recorded at the end of the measurement cycle, it is possible that an increase in background signal throughout a measurement cycle could also lead to a slight underestimation of the OH concentration.

Since the AMMA campaign, a diagnostic system coupling a fast photodiode (Hamamatsu, S6468) to an oscilloscope (Waverunner LT372, Le Croy) has been developed to monitor the timing of the CPM gate trigger relative to the laser pulse and not the laser

trigger. This technique allows the time between the laser pulse itself and the CPM gate trigger to be adjusted automatically in flight every 10 s, thus maintaining a constant time delay. A similar system is now used in the Leeds ground-based FAGE instrument and is described in detail in Whalley et al. (2009). Using this system, the sensitivity of the instrument to the time interval between the laser pulse and the fluorescence collection was investigated. Figure 7 shows how the background signal increases dramatically as the time between the laser pulse and fluorescence collection decreases and more of the laser pulse is detected. The limit of detection is also shown to worsen at shorter time intervals (Fig. 7).

Under normal operating conditions (delay of 60 ns), the instrumental LOD for OH ($\sim 7\times10^5$ molecule cm^{-3}) is below peak concentrations of OH observed in the tropics (e.g. [OH] = 9×10^6 molecule cm^{-3} observed at a tropical marine site in summer, Whalley et al., 2009). However, as the delay time decreases, the LOD becomes comparable to ambient concentrations of OH. Ambient concentrations of HO_2 are much greater than the HO_2 LOD (e.g. [HO_2] = 6×10^8 molecule cm^{-3}, Whalley et al., 2009) and the relative increase of HO_2 LOD compared to ambient concentrations has far less of an impact than for OH.

2.8 Ancillary measurements

$J(O^1D)$ was provided by the University of Leicester. $J(O^1D)$ is the combination of the upward and downward welling observations. During the campaign the downward welling $J(O^1D)$ actinometer failed and subsequent observations were scaled to the combined $J(NO_2)$ observations, as described in Stone et al. (2010). Core aircraft data such as temperature, pressure, CO (Aerolaser AL5002 instrument), O_3 (TECO 49UV photometery instrument) and liquid water content (Johnson Williams Liquid Water Content probe) were provided by the Facility of Airborne Atmospheric Measurements (FAAM) (Reeves et al., 2010), PAN data were provided by the University of York (Stewart et al., 2008) and NO_x, NO_y (Stewart et al., 2008), acetonitrile and

isoprene (Proton Transfer Mass Spectrometry – PTr-MS; Murphy et al., 2010) were provided by the University of East Anglia.

3 Results: observations of OH and HO_2 radicals

The Leeds aircraft FAGE instrument observed OH and HO_2 over a range of altitudes (500 m–9 km) and through various airmasses over West Africa. The observed signal was processed and the concentration of OH and HO_2 calculated using the instrument sensitivity determined by calibration, as described in Sect. 2.6. The 1 Hz mixing ratios of OH and HO_2 were calculated using the temperature and pressure recorded on the aircraft and averaged over 60 s. The 1 Hz HO_2 data were used directly in the study of HO_2 in clouds (Sect. 4.3).

HO_x observations were made on 13 flights during July and August 2006, with flights both during day and at night. Figure 8 shows the spatial distribution of HO_2 observed over West Africa during the AMMA campaign. The aircraft was based in Niamey, Niger and HO_x observations were made over barren soil in the north (Sahel region of northern Niger and Mali), over regions of forest (Benin) and out over the Gulf of Guinea to the south. An overview of the aircraft measurements can be found in Reeves et al. (2010).

Figure 9 is an example of a typical OH and HO_2 time series for a flight on 17 August 2006. The aircraft sampled between 500 m and 6 km over the forested region to the north of Benin (7–13° N). The O_3 mixing ratios were found to increase with altitude. OH mixing ratios were generally above the limit of detection and HO_2 mixing ratios were found to be highly variable on a 10 s time scale. At the level run at 1.5 km, light cloud was encountered and HO_2 mixing ratios were found to rapidly decrease. This will be studied in more detail in Sect. 4.3.

Overall during the campaign, the mixing ratios of OH and HO_2 were variable. Figure 10 shows the probability density function of the complete dataset of OH and HO_2 mixing ratios, with the median of the limit of detection. OH mixing ratios (Fig. 10a) from

−0.27 pptv to 1.34 pptv were observed (but with very few points above 1 pptv) and the most probable value was observed at 0.15 pptv. HO_2 mixing ratios (Fig. 10b) varied from −0.32 pptv to 42.65 pptv, with the highest frequency observed at 1.5 pptv. For significant periods, the OH observations were close to the limit of detection of the instrument due to problems with the instability of the timing of the fluorescence detection (as discussed in Sect. 2.7). However, as most HO_2 is well above the limit of detection, conclusions can be drawn with more confidence.

3.1 Diurnal variation

Although complex mechanisms determine the in situ concentrations of OH and HO_2, daytime OH production is generally dominated by the photolysis of ozone and often exhibits a strong diurnal profile (Rohrer and Berresheim, 2006). Figure 11 shows the diurnal profile of the entire dataset of OH and HO_2 radicals as a function of local solar time. Both OH and HO_2 were highly variable throughout the day, with the maximum OH mixing ratio (∼1 pptv) coinciding with solar noon, while maximum HO_2 mixing ratio (40 pptv) occurred shortly after solar noon. Mixing ratios of HO_2 up to 9 pptv with a mean of 3 pptv were observed at night. The observations of HO_2 at night will be discussed in detail in Sect. 4.4.

3.2 HO_x observations as a function of altitude

Figure 12 shows the daytime altitude profiles of (a) OH, (b) HO_2 and (c) the HO_2/OH ratio for data between 09:00 and 15:00 LT (Local Time), with the median value for a given 500 m altitude bin also shown.

OH mixing ratios (binned for 500 m altitude bins up to 6 km) are highly variable but the median OH is relatively constant with altitude at about 0.2 pptv, except for a large increase at the top of the boundary layer at 2 km to 0.7 pptv and distinct decrease at 5 km to less than 0.05 pptv. These observations of OH compare well with previous OH observations made using other instruments. Observations over the mid-latitude

and tropical Pacific Ocean found that median OH was relatively constant with altitude at ∼0.1–0.2 pptv, increasing from ∼0.1 pptv below 2 km to ∼0.2 pptv at 7 km (INTEX-B and PEM-Tropics-B campaigns, Mao et al., 2009; Tan et al., 2001, respectively). Over continental mid-latitudes, median OH was again relatively constant at all altitudes but at a slightly higher mixing ratio at ∼0.2–0.3 pptv (INTEX-A campaign, Ren et al., 2008). However, boundary layer OH mixing ratios varied significantly from 0.01–0.6 pptv. Observations over a tropical forested region (GABRIEL campaign, Martinez et al., 2008) found much higher OH mixing ratios with median OH increasing from ≈0.4 pptv in the boundary layer, peaking at 0.75 pptv at 3–4 km and dropping to ∼0.25 pptv at 8 km.

HO_2 mixing ratios were also variable at all altitudes and median HO_2 varied between 5 and 30 pptv for 500 m altitude bins up to 7 km. The lowest observed mixing ratios of HO_2 were found within 500 m of the forest surface, but the highest HO_2 mixing ratios were observed between 500 m and 1 km above the forest. At altitudes above 6 km, individual HO_2 data points varied from below the limit of detection to over 30 pptv HO_2, with a median value of ∼5 pptv. Previous observations of HO_2 generally show a decrease with altitude in all locations. Over the mid-latitude North Pacific HO_2 steadily decreased from ∼20 pptv at 2 km to ∼7 pptv at 10 km (INTEX-B campaign, Mao et al., 2009), while over continental mid-latitudes, median HO_2 steadily decreased from ∼30 pptv near the surface (ranging from ∼2–60 pptv) to ∼10 pptv at 10 km (INTEX-A campaign, Ren et al., 2008) and over tropical rainforests median HO_2 was found to decrease from ∼40 pptv in the boundary layer to ∼10 pptv at 8 km (GABRIEL campaign, Martinez et al., 2008). However, observations over the tropical south Pacific Ocean show a slightly different profile; HO_2 increased from ∼10 pptv at the surface to ∼20 pptv at 3 km before steadily decreasing again with altitude to ∼5 pptv at 11 km (PEM-Tropics-B campaign, Tan et al., 2001).

The HO_2/OH ratio was highly variable at all altitudes, ranging from 5 to 5 000 with a median value of 95. While HO_x production is dominated by O_3 photolysis, the cycling between OH and HO_2 is closely related to the abundance of CO and NO present (Ehhalt, 1999). At the altitudes considered here, overall O_3 varied between 10 and

100 ppbv and median values gradually increased with altitude to 7 km. CO varied between 50 and 450 ppbv, but overall decreased slightly with altitude (Reeves et al., 2010). Median NO and total NO_x both decreased with altitude to the top of the boundary layer (2 km). Total NO_x is constant with altitude from 2 to 7 km, while NO increases slightly above 5.5 km (Stewart et al., 2008).

3.3 Steady state calculations

As discussed earlier, the photolysis of ozone in the presence of water vapour is the main production pathway of OH in the unpolluted troposphere (Eq. 1). Figure 13 shows the correlation between OH and P(OH). OH mixing ratios were highly variable but were generally found to increase with increasing P(OH). In contrast to here, previous observations at ground sites with relatively constant OH sinks, found that the observed variation in OH was largely explained by corresponding variations in P(OH) (Rohrer and Berresheim, 2006).

In a clean airmass, the production of HO_2 is closely linked to P(OH) and the loss is dominated by the HO_2 self reaction:

$$HO_2 + HO_2 \longrightarrow H_2O_2 + O_2 \qquad \text{(R7)}$$

Assuming this production of HO_2 (~P(OH)) and loss of HO_2 through self-reaction (Reaction R7) are equal, a steady state concentration in clean air, $HO_{2\,ss}$, can be calculated:

$$HO_{2\,ss} = \sqrt{\frac{P(OH)}{2\,k_{R7}}} = \sqrt{\frac{2\,J(O^1D)\,[O_3]\,F_{OH}}{2\,k_{HO_2+HO_2}}} \qquad (11)$$

Figure 14 shows that $HO_{2\,ss}$ correlates well with the observed HO_2 (R=0.57) and the slope of 0.61 indicates that overall $HO_{2\,ss}$ is overestimating HO_2, suggesting missing sinks of HO_2. This is not unexpected, given that the rapid loss of HO_2 by reaction with species such as RO_2 or NO_2 or other sinks of HO_x radicals such as heterogeneous chemistry. From Fig. 14, a number of distinct groups have been identified. HO_2

is generally reproduced by $HO_{2\ ss}$ in areas of high mixing ratios of isoprene (green) (Sect. 4.1). However, the $HO_2/HO_{2\ ss}$ ratio is much less for observations in a biomass burning plume, suggesting the presence of significant HO_2 sinks (Sect. 4.2). Stone et al. (2010) describe how the observed photolysis rates were generally slightly lower than calculated from the Tropospheric Ultraviolet and Visible (TUV) Radiation model. However, on part of one particular flight (B228, shown in white in Fig. 14) the observations exceeded the calculated $J(O^1D)$ by a factor of 1.5. Thus, it is possible that the P(OH) calculated at this time is significantly overestimated.

This simple analysis is suitable for the examination of the overall HO_x behaviour but detailed interpretation requires a more comprehensive chemical modelling study. However, the comprehensive analysis of Stone et al. (2010) implies that, for much of the air over tropical West Africa, the HO_2 concentrations is controlled by relatively simple processes.

4 Discussion

A number of case studies have been identified in Sect. 3 and will now be examined in detail. Compared with P(OH) and $HO_{2\ ss}$, both OH and HO_2 are enhanced in the presence of high isoprene (Sect. 4.1), but are depleted within a biomass burning plume (with acetonitrile higher than 250 pptv) (Sect. 4.2). A reduction in HO_2 was also observed when sampling in cloud (Sect. 4.3) and HO_2 was observed at night (Sect. 4.4).

4.1 OH and HO_2 with isoprene

Figure 15 shows the latitudinal variation of OH and HO_2 and highlights how the maximum mixing ratios of both OH and HO_2 were found in the boundary layer of the southern end of the forest region. The West African Monsoon (WAM) brings the majority of rainfall to the continent and produces a strong latitudinal gradient in vegetation and biogenic emissions such as isoprene: Murphy et al. (2010) show that the highest mixing

ratios of isoprene were observed in the boundary layer above the southern forest regions (9–11° N).

Modelling studies of the latitudinal gradient of West Africa predict minimal HO_x concentrations over the forested regions due to isoprene scavenging of OH (Saunois et al., 2009). Isoprene reacts quickly with OH ($k = 1.0 \times 10^{-10}$ cm^3 s^{-1} at 294 K; Karl et al., 2004) and, given the concentrations of isoprene in the boundary layer above forests, this reaction should result in significant depletion of OH.

However, the observations presented here suggest that neither OH nor HO_2 mixing ratios are significantly depleted. Lelieveld et al. (2008) also observed higher than expected mixing ratios of HO_x over forests in Suriname and suggested that additional production of OH from the degradation products of isoprene (Dillon and Crowley, 2008; Peeters et al., 2009; Paulot et al., 2009; da Silva et al., 2010) could explain the high concentrations of HO_x. Given the complex nature of the oxidation of VOCs, the interpretation of these HO_x mixing ratios requires a more comprehensive modelling study than presented here. Stone et al. (2010) presents a detailed chemical box modelling study, based on the master chemical mechanism, to explore the interpretation of the HO_x observations presented here.

4.2 Biomass burning plume

As highlighted in Figs. 13 and 14, OH and HO_2 sampled in a biomass burning plume showed some of the largest disagreement for the steady state calculations. The biomass burning plume was sampled at two altitudes over the Gulf of Guinea. At an alititude of 4–5 km, the mean O_3 mixing ratio was ~50 ppbv and the mean CO mixing ratio was 150 ppbv. At an altitude of 3.5 km, mixing ratios of O_3 and CO were some of the highest observed during the campaign (100 ppbv and 300 ppbv respectively). Coincident with these observations was a sharp increase in NO, acetonitrile (CH_3CN) and

Peroxyacetyl Nitrate (PAN). Acetonitrile has been identified as a tracer for airmasses affected by biomass burning (de Gouw et al., 2003).

Figure 16 shows the time series of O_3, CO, OH and P(OH) and HO_2 and $HO_{2\ ss}$. The biomass burning plume was sampled at two altitudes, with the highest concentrations of both O_3 and CO observed at an altitude of 3–4 km (indicated as BB between the blues dashed lines). Within the plume at 3.5 km , 400 pptv CH_3CN was observed (up from 100 pptv outside the plume) and 600 pptv PAN was observed (up from 50 pptv outside the plume). The increase in observed OH within the plume at 3.5 km compared to 4.5 km coincides with an increase in NO at the lower altitude. The calculation of $HO_{2\ ss}$ does not incorporate the loss of HO_x through reactions such as RO_2+HO_2, OH+VOC, OH+NO_2 or reactions with aerosols, so it is not surprising that $HO_{2\ ss}$ is significantly higher than the observed HO_2.

Previous observations of VOCs within aged biomass burning plumes (de Gouw et al., 2003) found that the OH inferred from the degradation of species such as benzene and toluene was a factor of 4 lower than that calculated by a OH climatology model (Spivakovsky et al., 2000). While Forberich et al. (1996) measured reduced levels of OH in a biomass burning plume on one afternoon, a systematic observation of oxidation in biomass burning plumes would help in our understanding of these events. Little biomass burning takes place in West Africa during the monsoon wet season and within the plume, NO mixing ratios reach a maximum of 200 pptv (NO_2 observations were not available at this time), while PAN mixing ratios increased to over 700 pptv, suggesting that this biomass burning plume was transported from the Southern Hemisphere (Thouret et al., 2009; Liousse et al., 2010).

In this plume, HO_2 mixing ratios are much lower than $HO_{2\ ss}$, as expected as $HO_{2\ ss}$ does not include all possible HO_x loss processes. The mixing ratios of a number of VOCs were observed to be greatly increased within the plume compared to outside the plume. Within the plume the greatest increase was observed in acetylene (factor of 7.5), followed by methanol (4.2), acetonitrile (3), benzene (2.9), ethane (2.9) and acetone (2.4). The CO mixing ratio increased from a mean of 98 ppbv outside the

plume to 245 ppbv within the plume. The rate of production of HO_2 from the OH reaction with CO can be compared to the rate of production of RO_2 through the reaction of OH with VOCs.

The reactivity of OH with various VOCs can be estimated as a fraction of the OH reactivity with CO:

$$R_{VOC} = \frac{\sum^{i} k_i[VOC]_i}{k_{CO+OH}}[CO] \quad (12)$$

where k_i is the rate constant for the reaction of the VOC_i with OH and $\sum^{i} k_i[VOC]_i$ is the sum over all the products of the VOC concentration and the appropriate rate coefficient for the reaction of OH with the VOC in question. From this ratio, the impact of enhanced VOC concentrations on OH can be examined. The reaction of OH with CO forms HO_2, thus conserving the HO_x budget. However, the reaction of OH with any of the VOCs enhanced in this plume does not immediately form HO_x and results in HO_x depletion. The VOC/CO ratio was found to be 1.6 times higher within the plume (71) than outside (43), consistent with the observed HO_x depletion within the plume.

4.3 HO_2 in cloud

When sampling in and around clouds, HO_2 was found to rapidly decrease for short episodes, before returning to the previous higher levels again. The background signal did not change when sampling around clouds, suggesting that this effect was not an instrumental artefact. Studies of a similar FAGE instrument have shown no response of the instrument sensitivity to aerosol loading (Whalley et al., 2010). Modelling studies have shown that gaseous HO_2 concentrations can be significantly reduced by aqueous phase chemistry, specifically through the efficient uptake of HO_2 onto cloud droplets (Tilgner et al., 2005). These aqueous phase models combine detailed microphysics and multiphase chemistry but few experimental observations exist to validate the model calculated depletion of radical species in clouds. Figure 17 shows the 1 s time series of

the observed HO_2, steady state calculated $HO_{2\ ss}$ mixing ratios and the Liquid Water Content (LWC, g m^{-3}) observed between 13:00 and 13:30 UTC at a constant altitude of 1.5 km over northern Benin (10.9–12.5° N) (Flight B235A, 17 August 2006). Figure 17 highlights how the timing of the short-lived reduction in HO_2 observed when sampling in cloud is reproduced by $HO_{2\ ss}$ but, as seen earlier, $HO_{2\ ss}$ is consistently greater than HO_2. Much of the variability in $HO_{2\ ss}$ is driven by changes in $J(O^1D)$, which varied greatly in and out of cloud, depending on the cloud thickness. O_3 was generally found to rapidly decrease in cloud, while the fraction of $O(^1D)$ reacting with H_2O vapour to form OH, F_{OH}, generally increased quickly due to higher water vapour, counteracting the decrease in ozone and $J(O^1D)$ to an extent. Overall these fast changes in P(OH) resulted in short-lived reductions in $HO_{2_{ss}}$. However, the observed reduction in HO_2 was much greater than that seen in $HO_{2\ ss}$. Thus the relative change in the $HO_2/HO_{2\ ss}$ ratio is considered for each cloud encounter, as this removes any variation due to changes in the HO_x production rates.

Figure 18a shows the 1 Hz time series of the $HO_2/HO_{2\ ss}$ ratio and the simultaneously observed liquid water content. The magnitude of the short-lived decreases in HO_2 inside the cloud are not reproduced in the calculated $HO_{2\ ss}$, resulting in a decrease in the $HO_2/HO_{2\ ss}$ ratio. These rapid decreases in the $HO_2/HO_{2\ ss}$ ratio generally coincide with increases in liquid water and may be due to the heterogeneous uptake of HO_2 onto the cloud aerosol surface. Figure 18b shows the $HO_2/HO_{2_{ss}}$ ratio as a function of liquid water content. While the values of $HO_2/HO_{2\ ss}$ ratio are highly variable, the highest ratios (median of 0.47) are found for low liquid water (below 0.2 g m^{-3}) and the lowest ratios (median of 0.25) are found for higher liquid water content (greater than 0.2 g m^{-3}).

The reduction in HO_2 in clouds has been observed previously using both FAGE and CIMS instruments (e.g. Mauldin et al., 1999; Olson et al., 2004) and this loss of HO_2 has been attributed to heterogeneous uptake of HO_2 onto the cloud aerosol. During the TRACE-P (Transport and Chemical Evolution over the Pacific) campaign, Olson et al. (2004) found that the observed HO_2 was much lower than that calculated by a

comprehensive chemistry model. For each 1 min data point, observations *within cloud* were identified. The observed-to-modelled HO_2 ratio was found to be significantly reduced when sampling clouds with an increased liquid water content but appeared to be independent of the duration of cloud sampling. The time resolution of many species required to calculate HO_2 in chemical models is too low to interpret the short-lived depletions in HO_2 observed during AMMA (e.g. minimum 15 s for isoprene observed by PTR-MS). Therefore these rapid reductions in HO_2 are unlikely to provide any more than a qualitative sense of the heterogeneous uptake of HO_2 by cloud droplets.

The impact of HO_2 loss due to uptake on liquid cloud was investigated. The first order loss to surfaces was calculated with the diffusion of cloud droplets included (Schwartz, 1984):

$$k'_{\text{loss}} = \frac{A}{\frac{4}{c_g \gamma} + \frac{r}{D_g}} \tag{13}$$

where k'_{loss} is the rate constant for the loss of HO_2 to cloud droplets (s^{-1}), A is the cloud droplet surface area per unit volume ($m^2\,m^{-3}$), γ is the uptake coefficient to liquid water, r is the droplet radius (m) and D_g is the diffusion coefficient (for cloud droplets $\sim 1\times10^{-6}\,m^2\,s^{-1}$, Ravishankara, 1997). The uptake of HO_2 onto cloud is not tightly constrained and the uptake coefficient is thought to vary between 0.1 and 1 (Jacob, 2000; Morita et al., 2004). The mean molecular speed of the gas, c_g ($m\,s^{-1}$) is:

$$c_g = \sqrt{\frac{8\,RT}{\pi M_w}} \tag{14}$$

where R is the universal gas constant, T is the temperature and M_w is the molecular weight of HO_2.

Unfortunately no information was available on the size or number concentration of cloud droplets encountered for the observation period examined here but the HO_x observations were made over the continent of West Africa and typical continental values

of cloud droplet size (10 µm) and concentration (1.5×10^8 droplets m^{-3}) have been assumed in the calculation of k'_{loss} (Wallace and Hobbs, 2002). The main production and loss mechanisms of HO_2 were calculated for all HO_2 data where the liquid water content was greater than 0.2 g m^{-3} and an assumed mid-range γ of 0.5.

Using these constraints, the mean rate of HO_2 loss to cloud droplets was calculated to be 4.2×10^6 molecule cm^{-3} s^{-1}, slightly greater than the primary production rate (4.1×10^6 molecule cm^{-3} s^{-1}) but much larger than the HO_2 self reaction (0.89×10^6 molecule cm^{-3} s^{-1}). Therefore it is reasonable to assume that the uptake of HO_2 onto cloud droplets is a major sink of HO_2 within a cloud. Without the inclusion of HO_2 uptake on clouds, the mean steady state calculated HO_2 mixing ratio, $HO_{2\ ss}$, is 35 pptv, much higher than the observed mean HO_2 mixing ratio of 10.6 pptv. It is possible to calculate a cloud-influenced HO_2 mixing ratio, $HO_{2\ cloud}$, assuming that the primary production of HO_2 (through OH) is equal to the loss of HO_2 from both self reaction and uptake on clouds:

$$P(OH) = k'_{loss}[HO_2] + 2\ k_{HO_2+HO_2}\ [HO_2]^2 \quad (15)$$

With the inclusion of HO_2 uptake onto cloud droplets in the calculation of HO_2, the mean $HO_{2\ cloud}$ mixing ratio was calculated to be 8.84 pptv, in closer agreement with the mean observed HO_2 mixing ratio (10.6 pptv), than the previous steady state calculation of 35 pptv. It is possible that the accurate knowledge of the cloud droplet size and concentration and better understanding of γ would improve agreement even further. Therefore in order to fully understand the role of clouds on the oxidative capacity of the troposphere, a more comprehensive field study of HO_2 and the properties of cloud droplets is required.

4.4 HO_2 at night

HO_2 was observed at night on a number of flights. A maximum HO_2 mixing ratio of 9.2 pptv was observed in the hour after sunset and a median HO_2 mixing ratio of

2.2 pptv observed overall at night. Figure 19 shows the time series of HO_2 after sunset, showing that HO_2 mixing ratios decrease as the night progresses, with the suggestion of an increase again just before dawn.

At night HO_2 can be generated from the ozonolysis of alkenes, (e.g. isoprene) and terpenes. Isoprene emissions are strongly dependent on sunlight, unlike terpene emissions which are also a function of temperature (Guenther et al., 2006). When night-time temperatures remain high, terpene emission may continue into the night and the reaction of these alkenes and terpenes with ozone leads to the production of HO_x. Mixing ratios of HO_2 in excess of that reported here have been observed at night previously at surface sites (e.g. 1–4 pptv HO_2 was observed in mid-latitude deciduous forest (Faloona et al., 2001), up to 10 pptv HO_2 was observed on Rishiri Island, Japan, (Kanaya et al., 2002) and over 10 pptv HO_2 observed in China, (Hofzumahaus et al., 2009)). However, to the best of our knowledge, no altitude profiles of night-time HO_2 have been reported previously.

Figure 20 shows the altitude profile of (a) HO_2 (pptv), and (b) O_3 (ppbv) observed at night. The greatest HO_2 mixing ratio observed (less than an hour after dusk) was within 500 m of the surface. O_3 mixing ratios were lowest (<20 pptv) at the surface and increased steadily with altitude through the boundary layer. Isoprene, emitted from the surface, and Methyl Vinyl Ketone (MVK), a degradation product of isoprene, were highest in the boundary layer and generally decreased with altitude. This suggests that alkene ozonolysis may play a role as a source of HO_2 at night in the forest boundary layer. Between 6 and 8 km, both isoprene and MVK were observed to increase slightly. As there is no source of isoprene at these altitudes, these species may have been convectively injected into the mid troposphere (Murphy et al., 2010), resulting in the production of HO_2 at higher altitude at night.

5 Conclusions

The Leeds aircraft FAGE instrument successfully measured tropospheric OH and HO_2 over west Africa during the summer monsoon in 2006. The instrument was deployed aboard the BAe-146 research aircraft as part of the African Monsoon Multidisciplinary Analyses (AMMA) campaign. For calibrations, known concentrations of HO_x were generated by the photolysis of water vapour by mercury lamp, with the lamp flux determined by NO actinometry. The instrument sensitivity did not change appreciably over the pressure range observed in the fluorescence cell during the campaign (1.5–2.1 Torr). The mean instrumental limit of detection observed during the campaign was 7.1×10^5 molecule cm^{-3} for OH (60 s integration time) and 7.5×10^5 molecule cm^{-3} for HO_2 (60 s integration time).

HO_x observations were made during 13 flights, ranging from 50 m to over 9 km. The aircraft sampled air over the Sahel (18° N), forest (8–12° N) and out over the ocean (4° N). OH and HO_2 mixing ratios show a diurnal profile but were highly variable. Observations of OH and HO_2 were compared with steady state calculation of HO_x and differences highlighted a number of case studies. High mixing ratios of OH and HO_2 were observed in areas of high isoprene, in sharp contrast to the depletion calculated by models. Within a biomass burning plume, HO_x was found to be depleted. Calculations show that OH was 1.6 times more likely to react with VOCs than CO, resulting in the observed depletion of HO_x. HO_2 data recorded at 1 Hz showed evidence of short-lived reductions in the observed HO_2 in and around cloud, which could not be explained by changing primary production rates within the cloud. The heterogeneous uptake of HO_2 onto the cloud surface was included in the steady state HO_x calculation and improved the agreement with the observed short-lived reductions of HO_2 in cloud. However, a more comprehensive field study of HO_2 and the properties of cloud droplets is required to fully understand the role of clouds on the oxidative capacity of the troposphere. Mixing ratios of HO_2 of 9 pptv were observed at night and the first

ACPD
10, 7265–7322, 2010

altitude profile of HO_2 at night is presented. Up to 7 pptv of HO_2 was observed above 6 km, consistent with the convective uplift of HO_2 precursors such as isoprene.

Acknowledgements. The authors would like to thank M. Darling and the staff of Avalon Aero for help in the integration of the instrument and Jack Fox and NCAR workshops for the design and manufacture of the inlet. Thanks to the staff of FAAM, Directflight and the AMMA AOC for all of their hard work in making the detachment possible. We would like to thank all of the scientists who worked on the BAe-146 for their hard work in making this project a success. We thank D. Brookes and P. Monks for providing $J(O^1D)$ data, J. Murphy and D. Oram for providing isoprene and acetonitrile data, D. Stewart for NO_x data, J. McQuaid for PAN data and A. Lewis, J. Lee and J. Hopkins for hydrocarbon data.

Based on a French initiative, AMMA was built by an international scientific group and was funded by a large number of agencies, especially from France, the UK, the US and Africa. This work was funded by the EU and by the UK Natural Environment Research Council through the AMMA-UK Consortium grant and the National Centre for Atmospheric Science.

References

Andres-Hernandez, M. D., Stone, D., Brookes, D. M., Commane, R., Reeves, C. E., Huntrieser, H., Heard, D. E., Monks, P. S., Burrows, J. P., Schlager, H., Kartal, D., Evans, M. J., Floquet, C. F. A., Ingham, T., Methven, J., Parker, A. E.: Peroxy radical partitioning during the AMMA intercomparison exercise, submitted, Atmos. Chem. Phys. Discuss., 2010. 7269

Bloss, W. J., Evans, M. J., Lee, J. D., Sommariva, R., Heard, D. E., and Pilling, M. J.: The oxidative capacity of the troposphere: Coupling of field measurements of OH and a global chemistry transport model, Faraday Discuss., 130, 130/22, 2005. 7268

Butler, T. M., Taraborrelli, D., Brühl, C., Fischer, H., Harder, H., Martinez, M., Williams, J., Lawrence, M. G., and Lelieveld, J.: Improved simulation of isoprene oxidation chemistry with the ECHAM5/MESSy chemistry-climate model: lessons from the GABRIEL airborne field campaign, Atmos. Chem. Phys., 8, 4529–4546, 2008, http://www.atmos-chem-phys.net/8/4529/2008/.

Capes, G., Murphy, J. G., Reeves, C. E., McQuaid, J. B., Hamilton, J. F., Hopkins, J. R., Crosier, J., Williams, P. I., and Coe, H.: Secondary organic aerosol from biogenic VOCs over West

Africa during AMMA, Atmos. Chem. Phys., 9, 3841–3850, 2009, http://www.atmos-chem-phys.net/9/3841/2009/. 7269

Cantrell, C. A., Shetter, R. E., Calvert, J. G., and Tanner, F. L. E. A. J.: Some considerations of the origin of nighttime peroxy radicals observed in MLOPEX, J. Geophys. Res.-Atmos., 102, 15899–15913, 1997. 7275

Creasey, D. J., Heard, D. E., and Lee, J. D.: Eastern Atlantic Spring Experiment 1997 (EASE97), 1. Measurements of OH and HO_2 concentrations at Mace Head, Ireland, J. Geophys. Res.-Atmos., 107, 4091, doi:10.1029/2001JD000892, 2002.

Crawford, J., Davis, D., Olson, J., Chen, G., Liu, S., Gregory, G., Barrick, J., Sachse, G., Sandholm, S., Heikes, B., Singh, H., and Blake, D.: Assessment of upper tropospheric HO_x sources over the tropical Pacific based on NASA GTE/PEM data: Net effect on HO_x and other photochemical parameters, J. Geophys. Res.-Atmos., 104, 16255–16273, 1999.

da Silva, G., Graham, C., and Wang, Z.-F.: Unimolecular β-Hydroxyperoxy Radical Decomposition with OH Recycling in the Photochemical Oxidation of Isoprene, Environ. Sci. Technol., 44, 250–256, 2010. 7285

de Gouw, J. A., Warneke, C., Parrish, D. D., Holloway, J. S., Trainer, M., and Fehsenfeld, F. C.: Emission sources and ocean uptake of acetonitrile (CH_3CN) in the atmosphere, J. Geophys. Res., 108, 4329, doi:10.1029/2002JD002897, 2003. 7286

Dillon, T. J. and Crowley, J. N.: Direct detection of OH formation in the reactions of HO_2 with $CH_3C(O)O_2$ and other substituted peroxy radicals, Atmos. Chem. Phys., 8, 4877–4889, 2008, http://www.atmos-chem-phys.net/8/4877/2008/. 7285

Dusanter, S., Vimal, D., Stevens, P. S., Volkamer, R., Molina, L. T., Baker, A., Meinardi, S., Blake, D., Sheehy, P., Merten, A., Zhang, R., Zheng, J., Fortner, E. C., Junkermann, W., Dubey, M., Rahn, T., Eichinger, B., Lewandowski, P., Prueger, J., and Holder, H.: Measurements of OH and HO_2 concentrations during the MCMA-2006 field campaign - Part 2: Model comparison and radical budget, Atmos. Chem. Phys., 9, 6655–6675, 2009, http://www.atmos-chem-phys.net/9/6655/2009/.

Edwards, G., Cantrell, C., Stephens, S., Hill, B., Goyea, O., Shetter, R., Mauldin, R., Kosciuch, E., Tanner, D., and Eisele, F.: Chemical Ionization Mass Spectrometer Instrument for the Measurement of Tropospheric HO_2 and RO_2, Anal. Chem., 75, 5317–5327, 2003. 7276

Ehhalt, D. H.: Photooxidation of trace gases in the troposphere, Phys. Chem. Chem. Phys., 1, 5401–5408, 1999. 7267, 7282

Eisele, F. L., Mauldin, R. L., Tanner, D. J., Fox, J. R., Mouch, T., and Scully, T.: An inlet/sampling duct for airborne OH and sulfuric acid measurements, J. Geophys. Res.-Atmos., 102, 27993–28001, 1997. 7270

Faloona, I., Tan, D., Brune, W., Hurst, J., Barket, D., Couch, T. L., Shepson, P., Apel, E., Riemer, D., Thornberry, T., Carroll, M. A., Sillman, S., Keeler, G. J., Sagady, J., Hooper, D., and Paterson, K.: Nighttime observations of anomalously high levels of hydroxyl radicals above a deciduous forest canopy, J. Geophys. Res.-Atmos., 106, 24315–24333, 2001. 7291

Faloona, I. C., Tan, D., Lesher, R. L., Hazen, N. L., Frame, C. L., Simpas, J. B., Harder, H., Martinez, M., Di Carlo, P., Ren, X., and Brune, W. H.: A laser induced fluorescence instrument for detecting tropospheric OH and HO_2: Characteristics and calibration, J. Atmos. Chem., 47, 139–167, 2004. 7274, 7276, 7277

Fehsenfeld, F., Calvert, J., Fall, R., Goldan, P., Guenther, A., Hewitt, C., Lamb, B., Liu, S., Trainer, M., Westberg, H., and Zimmerman, P.: Emissions of volatile organic compounds from vegetation and the implications for atmospheric chemistry., Global Biogeochem. Cy., 6, 389–430, 1992. 7268

Forberich, W. J. and Comes, F. J.: Measurement of OH concentration during a forest fire episode: atmospheric implications for biomass burning, Chem. Phys. Lett., 259, 408–414, doi:DOI:10.1016/0009-2614(96)00805-6, 1996. 7286

Fuentes, J. D., Lerdau, M., Atkinson, R., Baldocchi, D., Bottenheim, J. W., Ciccioli, P., Lamb, B., Geron, C., Gu, L., Guenther, A., Sharkey, T. D., and Stockwell, W.: Biogenic hydrocarbons in the atmospheric boundary layer: A review, B. Am. Meteorol. Soc., 81, 1537–1575, 2000. 7268

Glowacki, D. R., Goddard, A., Hemavibool, K., Malkin, T. L., Commane, R., Anderson, F., Bloss, W. J., Heard, D. E., Ingham, T., Pilling, M. J., and Seakins, P. W.: Design of and initial results from a Highly Instrumented Reactor for Atmospheric Chemistry (HIRAC), Atmos. Chem. Phys., 7, 5371–5390, 2007, http://www.atmos-chem-phys.net/7/5371/2007/. 7276

Guenther, A., Hewitt, N. C., Erickson, D., Fall, R., Geron, C., Graedel, T., Harley, P., Klinger, L., Lerdau, M., McKay, W. A., Pierce, T., Scholes, B., Steinbrecher, R., Tallamraju, R., Taylor, J., and Zimmerman, P.: A global model of natural volatile organic compound emissions, J. Geophys. Res.-Atmos., 100, 8873–8892, 1995. 7268

Guenther, A., Karl, T., Harley, P., Wiedinmyer, C., Palmer, P. I., and Geron, C.: Estimates of global terrestrial isoprene emissions using MEGAN (Model of Emissions of Gases and

Aerosols from Nature), Atmos. Chem. Phys., 6, 3181–3210, 2006, http://www.atmos-chem-phys.net/6/3181/2006/. 7268, 7291
Hard, T. M., O'Brien, R. J., Chan, C. Y., and Mehrabzadeh, A. A.: Tropospheric Free-Radical Determination by FAGE, Environ. Sci. Technol., 18, 768–777, 1984. 7269
Heard, D. E. and Pilling, M. J.: Measurement of OH and HO_2 in the Troposphere, Chem. Rev., 103, 5163–5198, 2003. 7268
Hofzumahaus, A., Rohrer, F., Lu, K., Bohn, B., Brauers, T., Chang, C.-C., Fuchs, H., Holland, F., Kita, K., Kondo, Y., Li, X., Lou, S., Shao, M., Zeng, L., Wahner, A., and Zhang, Y.: Amplified Trace Gas Removal in the Troposphere, Science, 324, 1702–1704, doi:10.1126/science.1164566, 2009. 7291
Holland, F., Hofzumahaus, A., Schafer, R., Kraus, A., and Patz, H. W.: Measurements of OH and HO_2 radical concentrations and photolysis frequencies during BERLIOZ, J. Geophys. Res.-Atmos., 108, 8246, doi:10.1029/2001JD001393, 2003.
Hopkins, J. R., Evans, M. J., Lee, J. D., Lewis, A. C., Marsham, J., McQuaid, J. B., Parker, D. J., Stewart, D. J., Reeves, C. E., and Purvis, R. M.: Direct estimates of emissions from the megacity of Lagos, Atmos. Chem. Phys., 9, 8471–8477, 2009, http://www.atmos-chem-phys.net/9/8471/2009/.
Hurst, J. M., Barket, D. J., Herrera-Gomez, O., Couch, T. L., Shepson, P. B., Faloona, I., Tan, D., Brune, W., Westberg, H., Lamb, B., Biesenthal, T., Young, V., Goldstein, A., Munger, J. W., Thornberry, T., and Carroll, M. A.: Investigation of the nighttime decay of isoprene, J. Geophys. Res.-Atmos., 106, 24335–24346, 2001.
Ingham, T., Vaughan, S., Commane, R., Edwards, P., Evans, M. J., Floquet, C. F. A., and Heard, D. E.: Aircraft instrument to measure OH and HO_2, Atmos. Meas. Tech. Discuss., in preparation, 2010. 7269, 7270
Jacob, D. J.: Heterogeneous chemistry and tropospheric ozone, Atmos. Environ., 34, 2131–2159, 2000. 7289
Kanaya, Y., Nakamura, K., Kato, S., Matsumoto, J., Tanimoto, H., and Akimoto, H.: Nighttime variations in HO_2 radical mixing ratios at Rishiri Island observed with elevated monoterpene mixing ratios, Atmos. Environ., 36, 4929–4940, 2002. 7291
Karl, M., Brauers, T., Dorn, H. P., Holland, F., Komenda, M., Poppe, D., Rohrer, F., Rupp, L., Schaub, A., and Wahner, A.: Kinetic Study of the OH-isoprene and O-isoprene reaction in the atmosphere simulation chamber, SAPHIR, Geophys. Res. Lett., 31, L05117, doi:10.1029/2003GL019189, 2004. 7285

Karl, T., Guenther, A., Yokelson, R. J., Greenberg, J., Potosnak, M., Blake, D. R., and Artaxo, P.: The Tropical forest and fire emissions experiment: Emission, Chemistry and transport of biogenic volatile organic compounds in the lower atmopsphere over Amazonia, J. Geophys. Res.-Atmos., 112, D18302, doi:10.1029/2007JD008539, 2007. 7268

Kesselmeier, J. and Staudt, M.: Biogenic volatile organic compounds (VOC): An overview on emission, physiology and ecology, J. Atmos. Chem., 33, 23–88, 1999. 7268

Kubistin, D., Harder, H., Martinez, M., Rudolf, M., Sander, R., Bozem, H., Eerdekens, G., Fischer, H., Gurk, C., Klüpfel, T., Königstedt, R., Parchatka, U., Schiller, C. L., Stickler, A., Taraborrelli, D., Williams, J., and Lelieveld, J.: Hydroxyl radicals in the tropical troposphere over the Suriname rainforest: comparison of measurements with the box model MECCA, Atmos. Chem. Phys. Discuss., 8, 15239–15289, 2008, http://www.atmos-chem-phys-discuss.net/8/15239/2008/. 7269

Lelieveld, J., Butler, T. M., Crowley, J. N., Dillon, T. J., Fischer, H., Ganzeveld, L., Harder, H., Lawrence, M. G., Martinez, M., Taraborrelli, D., and Williams, J.: Atmospheric oxidation capacity sustained by a tropical forest, Nature, 452, 737–740, doi:10.1038/nature06870, 2008. 7268, 7285

Lelieveld, J., Peters, V., Dentener, F. J., and Krol, M.: Stability of tropospheric hydroxyl chemistry, J. Geophys. Res., 107(D23), 4715, doi:10.1029/2002JD002272, 2002. 7268

Liousse, C., Guillaume, B., Grégoire, J. M., Mallet, M., Galy, C., Poirson, A., Solmon, F., Pont, V., Mariscal, A., Dungal, L., Rosset, R., Yoboué, V., Bedou, X., Sera, D., Konaré, A., Granier, C., and Mieville, A.: African aerosols modeling during the EOP-AMMA campaign with updated biomass burning emission inventories, Atmos. Chem. Phys. Discuss., submitted, 2010. 7286

Mao, J., Ren, X., Brune, W. H., Olson, J. R., Crawford, J. H., Fried, A., Huey, L. G., Cohen, R. C., Heikes, B., Singh, H. B., Blake, D. R., Sachse, G. W., Diskin, G. S., Hall, S. R., and Shetter, R. E.: Airborne measurement of OH reactivity during INTEX-B, Atmos. Chem. Phys., 9, 163–173, 2009, http://www.atmos-chem-phys.net/9/163/2009/. 7268, 7282

Mari, C. H., Cailley, G., Corre, L., Saunois, M., Attié, J. L., Thouret, V., and Stohl, A.: Tracing biomass burning plumes from the Southern Hemisphere during the AMMA 2006 wet season experiment, Atmos. Chem. Phys., 8, 3951–3961, 2008, http://www.atmos-chem-phys.net/8/3951/2008/.

Martinez, M., Harder, H., Kubistin, D., Rudolf, M., Bozem, H., Eerdekens, G., Fischer, H., Gurk, C., Klüpfel, T., Königstedt, R., Parchatka, U., Schiller, C. L., Stickler, A., Williams, J.,

and Lelieveld, J.: Hydroxyl radicals in the tropical troposphere over the Suriname rainforest: airborne measurements, Atmos. Chem. Phys. Discuss., 8, 15491–15536, 2008, http://www.atmos-chem-phys-discuss.net/8/15491/2008/. 7269, 7275, 7277, 7282

Mauldin, R. L., Tanner, D. J., and Eisele, F. L.: Measurements of OH during PEM-Tropics A, J. Geophys. Res.-Atmos., 104, 5817–5827, 1999. 7288

Morita, A., Kanaya, Y., and Francisco, J. S.: Uptake of the HO_2 radical by water: Molecular dynamics calculations and their implications for atmospheric modeling, J. Geophys. Res., 109, D09201, doi:10.1029/2003JD004240, 2004. 7289

Murphy, J. G., Oram, D. E., and Reeves, C. E.: Measurements of volatile organic compounds over West Africa, Atmos. Chem. Phys. Discuss., 10, 3861–3892, 2010, http://www.atmos-chem-phys-discuss.net/10/3861/2010/. 7280, 7284, 7291

Olson, J. R., Crawford, J. H., Chen, G., Fried, A., Jordan, M. J. E. C. E., Sandholm, S. T., Davis, D. D., Avery, B. E. A. M. A., Barrick, J. D., Blake, D. R., Brune, W. H., Eisele, F. L., Flocke, F., Harder, H., Jacob, D. J., Lefer, Y. K. A. L., Martinez, M., Mauldin, R. L., Sachse, G. W., Shetter, R., Singh, H. B., Talbot, R. W., and Tan, D.: Testing fast photochemical theory during TRACE-P based on measurements of OH, HO_2 and CH_2O, J. Geophys. Res.-Atmos., 109, D15S10, doi:10.1029/2003JD004278, 2004. 7288

Paulot, F., Crounse, J. D., Kjaergaard, H. G., Kurten, A., St. Clair, J. M., Seinfeld, J. H., and Wennberg, P. O.: Unexpected Epoxide Formation in the Gas-Phase Photooxidation of Isoprene, Science, 325, 730, doi:10.1126/science.1172910, 2009. 7285

Peeters, J., Nguyen, T. J., and Vereecken, L.,: HO_x radical regeneration in the oxidation of isoprene, Phys. Chem. Chem. Phys., 11, 5935–5939, 2009. 7285

Poisson, N., Kanakaidou, M., and Crutzen, P.: Impact of Non-Methane Hydrocarbons on Tropospheric Chemistry and the Oxidizing Power of the Global Troposphere: 3-Dimensional Modelling Results, J. Atmos. Chem., 36, 157–230, 2000. 7268

Ravishankara, A. R.: Heterogeneous and multiphase chemistry in the troposphere, Science, 276, 1058–1065, Science, 1997. 7289

Reeves, C. E., Formenti, P., Afif, C., Ancellet, G., Attie, J.-L., Bechara, J., Borbon, A., Cairo, F., Coe, H., Crumeyrolle, S., Fierli, F., Flamant, C., Gomes, L., Hamburger, T., Lambert, C., Law, K. S., Mari, C., Matsuki, A., Methven, J., Mills, G. P., Minikin, A., Murphy, J. G., Nielsen, J. K., Oram, D. E., Parker, D. J., Richter, A., Schlager, H., Schwarzenboeck, A., and Thouret, V.: Chemical and aerosol characterisation of the troposphere over West Africa during the monsoon period as part of AMMA, Atmos. Chem. Phys. Discuss., 10, 7115–7183, 2010,

http://www.atmos-chem-phys-discuss.net/10/7115/2010/. 7269, 7279, 7280, 7283
Ren, X. R., Brune, W., Cantrell, C., Edwards, G., Shirley, T., Metcalf, A., and Lesher, R.: Hydroxyl and peroxy radical chemistry in a rural area of Central Pennsylvania: Observations and model comparisons, J. Atmos. Chem., 52, 231–257, 2005.
Ren, X., Olson, J. R., Crawford, J. H., Brune, W. H., Mao, J., Long, R. B., Chen, Z., Chen, G., Avery, M. A., Sachse, G. W., Barrick, J. D., Diskin, G. S., Huey, L. G., Fried, A., Cohen, R. C., Heikes, B., Wennberg, P. O., Singh, H. B., Blake, D. R., and Shetter, R. E.: HO_x chemistry during INTEX-A 2004: Observation, model calculation, and comparison with previous studies, J. Geophys. Res., 113, D05310, doi:10.1029/2007JD009166, 2008. 7282
Rohrer, F. and Berresheim, H.: Strong correlation between levels of tropospheric hydroxyl radicals and solar ultraviolet radiation, Nature, 442, 184–187, 2006. 7281, 7283
Sander, S. P., Friedl, R. R., Golden, D. M., Kurylo, M. J., Moortgat, C. K., Keller-Rudek, H., Wine, P. H., Ravishankara, A. R., Kolb, C. E., Molina, M. J., Finlayson-Pitts, B. J., Orkin, V. L., and Huie, R. E.: Chemical kinetics and photochemical data for use in stratospheric studies, Evaluation number 15, NASA Jet Propulsion Laboratory, Publication 06-2, 2006.
Saunders, S. M., Jenkin, M. E., Derwent, R. G., and Pilling, M. J.: Protocol for the development of the Master Chemical Mechanism, MCM v3 (Part A): tropospheric degradation of non-aromatic volatile organic compounds, Atmos. Chem. Phys., 3, 161–180, 2003, http://www.atmos-chem-phys.net/3/161/2003/.
Saunois, M., Reeves, C. E., Mari, C. H., Murphy, J. G., Stewart, D. J., Mills, G. P., Oram, D. E., and Purvis, R. M.: Factors controlling the distribution of ozone in the West African lower troposphere during the AMMA (African Monsoon Multidisciplinary Analysis) wet season campaign, Atmos. Chem. Phys., 9, 6135–6155, 2009, http://www.atmos-chem-phys.net/9/6135/2009/. 7285
Schwartz, S. E.: Gas- and Aqueous-Phase Chemistry of HO_2 in Liquid Water Clouds, J. Geophys. Res., 89, 11589–11598, 1984. 7289
Smith, S. C., Lee, J. D., Bloss, W. J., Johnson, G. P., Ingham, T., and Heard, D. E.: Concentrations of OH and HO_2 radicals during NAMBLEX: measurements and steady state analysis, Atmos. Chem. Phys., 6, 1435–1453, 2006, http://www.atmos-chem-phys.net/6/1435/2006/. 7276
Spivakovsky, C. M., Logan, J. A., Montzka, S. A., Balkanski, Y. J., Foreman-Fowler, M., Jones, D. B. A., Horowitz, L. W., Fusco, A. C., Brenninkmeijer, C. A. M., Prather, M. J., Wofsy, S. C., and McElroy, M. B.: Three-dimensional climatological distribution of tropospheric OH:

Update and evaluation, J. Geophys. Res.-Atmos., 105, 8931–8980, 2000. 7286

Stevens, P. S., Mather, J. H., and Brune, W. H.: Measurement of Tropospheric OH and HO_2 by Laser-Induced Fluorescence at Low-Pressure, J. Geophys. Res.-Atmos., 99, 3543–3557, 1994. 7272, 7277

Stewart, D. J., Taylor, C. M., Reeves, C. E., and McQuaid, J. B.: Biogenic nitrogen oxide emissions from soils: impact on NO_x and ozone over west Africa during AMMA (African Monsoon Multidisciplinary Analysis): observational study, Atmos. Chem. Phys., 8, 2285–2297, 2008, http://www.atmos-chem-phys.net/8/2285/2008/. 7269, 7279, 7283

Stone, D., Commane, R., Floquet, C. F. A., Ingham, T., Bandy, B., Brookes, D., Hopkins, J., Lee, J., Lewis, A., McQuaid, J., Mills, G., Monks, P., Murphy, J., Oram, D., Parker, A., Purvis, R., Reeves, C., Stewart, D., Heard, D. E., and Evans, M. J.: Understanding HO_x observations over West Africa during AMMA: Box modelling with the MCM, Atmos. Chem. Phys. Discuss., in preparation, 2010. 7269, 7279, 7284, 7285

Tan, D., Faloona, I., Simpas, J. B., Brune, W., Olson, J., Crawford, J., Avery, M., Sachse, G., Vay, S., Sandholm, S., Guan, H. W., Vaughn, T., Mastromarino, J., Heikes, B., Snow, J., Podolske, J., and Singh, H.: OH and HO_2 in the tropical Pacific: Results from PEM-Tropics B, J. Geophys. Res.-Atmos., 106, 32667–32681, 2001. 7268, 7282

Thouret, V., Saunois, M., Minga, A., Mariscal, A., Sauvage, B., Solete, A., Agbangla, D., Nédélec, P., Mari, C., Reeves, C. E., and Schlager, H.: An overview of two years of ozone radio soundings over Cotonou as part of AMMA, Atmos. Chem. Phys., 9, 6157–6174, 2009, http://www.atmos-chem-phys.net/9/6157/2009/. 7286

Tilgner, A., Majdik, Z., Sehili, A. M., Simmel, M., Wolke, R., and Herrmann, H.: SPACCIM: Simulations of the multiphase chemistry occurring in the FEBUKO hill cap cloud experiments, Atmos. Environ., 39, 4389–4401, 2005. 7287

von Kuhlmann, R., Lawrence, M. G., Pöschl, U., and Crutzen, P. J.: Sensitivities in global scale modeling of isoprene, Atmos. Chem. Phys., 4, 1–17, 2004, http://www.atmos-chem-phys.net/4/1/2004/. 7268

Wallace, J. M. and Hobbs, P. V.: Atmospheric Science: An Introductory Survey, Academic Press, 2002. 7290

Weinstock, B.: Carbon monoxide: Residence time in the atmosphere, Science, 168, 224–225, 1969. 7267

Wennberg, P. O., Cohen, R. C., Hazen, N. L., Lapson, L. B., Allen, N. T., Hanisco, T. F., Oliver, J. F., Lanham, N. W., Demusz, J. N., and Anderson, J. G.: Aircraft-borne laser induced fluorescence instrument for the in situ detection of hydroxyl and hydroperoxy radicals, Rev. Sci. Instrum., 65, 1858–1876, 1994. 7272

Whalley, L. K., Baeza-Romero, M. T., George, I., Brooks, B., and Heard, D. E.: Do ambient aerosols influence the sensitivity of laser-induced fluorescence instruments for the measurement of tropospheric OH and HO_2 radicals?, Atmos. Meas. Tech. Discuss., in preparation, 2010. 7287

Whalley, L. K., Furneaux, K. L., Goddard, A., Lee, J. D., Mahajan, A., Oetjen, H., Read, K. A., Kaaden, N., Carpenter, L. J., Lewis, A. C., Plane, J. M. C., Saltzman, E. S., Wiedensohler, A., and Heard, D. E.: The chemistry of OH and HO_2 radicals in the boundary layer over the tropical Atlantic Ocean, Atmos. Chem. Phys., 10, 1555–1576, 2010, http://www.atmos-chem-phys.net/10/1555/2010/. 7268, 7279

Whalley, L. K., Furneaux, K. L., Gravestock, T., Atkinson, H. M., Bale, C. S. E., Ingham, T., Bloss, W. J., and Heard, D. E.: Detection of Iodine Monoxide Radicals in the Marine Boundary Layer using Laser Induced Fluorescence Spectroscopy, J. Atmos. Chem., 58, 19–39, 2007. 7276

Table 1. Limit Of Detection (LOD) for a 60 s integration calculated for a typical run on 17 August 2006.

Parameter	OH	HO_2
$T_{69\%}$	1	1
P/mW	10.7	5.7
C_{HO_x} (10^{-7} cts s^{-1} mW^{-1} molecule^{-1} cm^3)	0.63	1.17
m	1	1
n	1	1
σ_{bg}/cts s^{-1}	8.1	33.9
$[HO_x]_{min}$ (10^6 molecule cm^{-3})	0.6	1.2

ACPD
10, 7265–7322, 2010

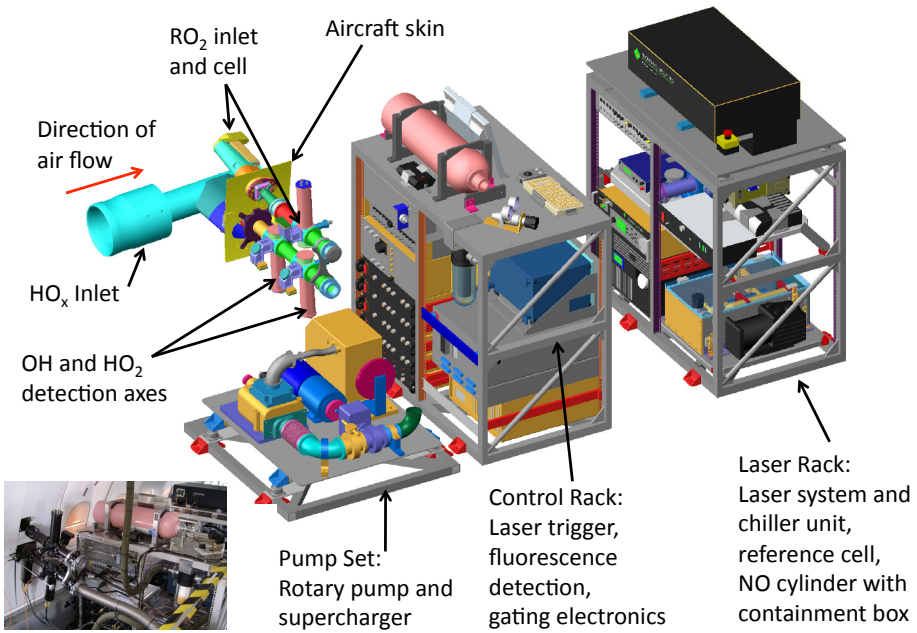

Fig. 1. Schematic outline of the Leeds FAGE instrument. Individual components are detailed in the text. The inlet delivers air to the fluorescence cell with OH and HO_2 detection axes. The cell is maintained at low pressure (1.5–2.1 Torr) by a rotary pump backed by a supercharger (Pump Set). The fluorescence cell and pump set are not joined for clarity. The Control Rack contains the instrument computer with photon counting cards, the photomultiplier power supplies and gating electronics, the laser trigger module and a nitrogen cylinder. The Laser Rack holds the YAG pumped Ti:Sapphire laser and chiller unit, the reference cell and a B2 size NO cylinder for HO_2 measurements. The NO cylinder is housed in a containment box designed to prevent any NO leak in the aircraft cabin in case of failure of the cylinder or regulator. Fibre optic cables (not shown) deliver the laser light from the laser to the OH, HO_2 and reference cells. An inlet and fluorescence cell for the detection of RO_2 have been fitted but are not yet operational.

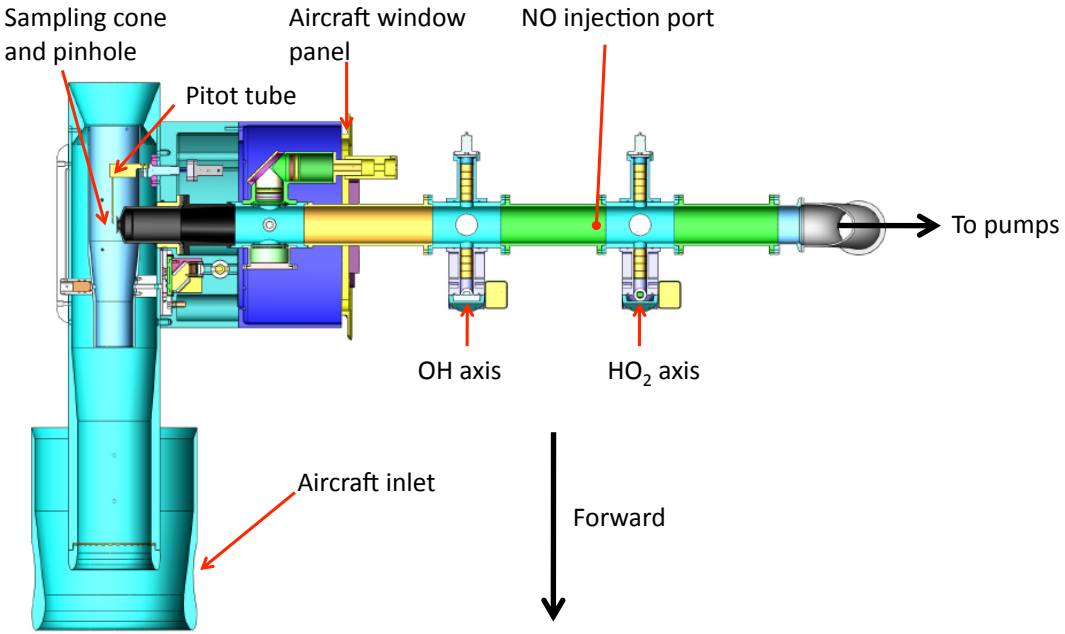

Fig. 2. Fluorescence cell for the sequential detection of OH and HO_2. OH is detected in the first axis, with fluorescence collected perpendicular to the laser beam and sample flow. NO is then injected to titrate HO_2 to OH and the signal due to HO_2 is detected in the HO_2 axis with fluorescence collection also perpendicular to the laser axis and sample flow.

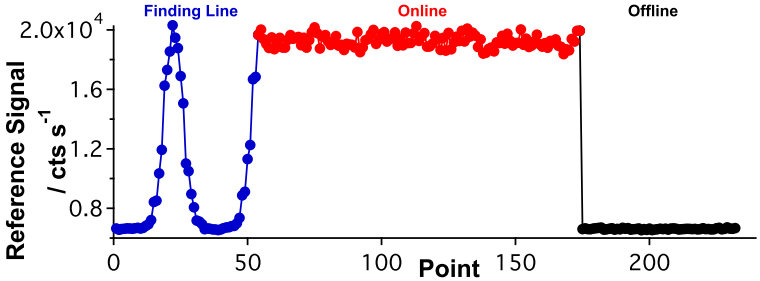

Fig. 3. Signal observed in the reference cell for a two minute measurement cycle. The $Q_1(2)$ rotational line is scanned over ("finding line", points 1–54, blue). Online (points ~55–175, red) represents the online measurement period. Offline (points 175–235, black) represents the background signal to be removed in the analysis. A 2.2% (1 σ) variation in reference signal is observed online.

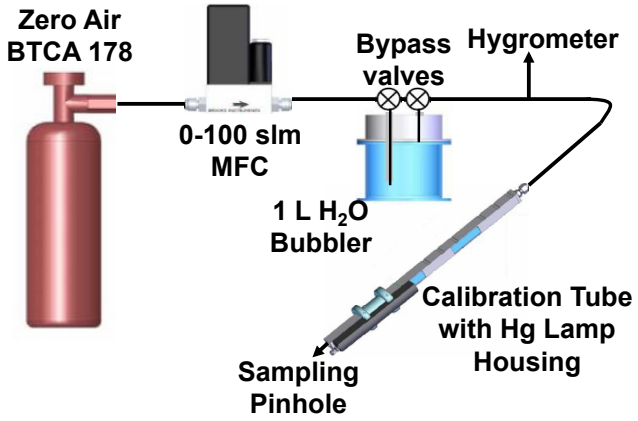

Fig. 4. Experimental setup of the calibration system. Zero air is humidified and passed through the calibration tube, where it is photolysed to produce a known concentration of OH and HO_2.

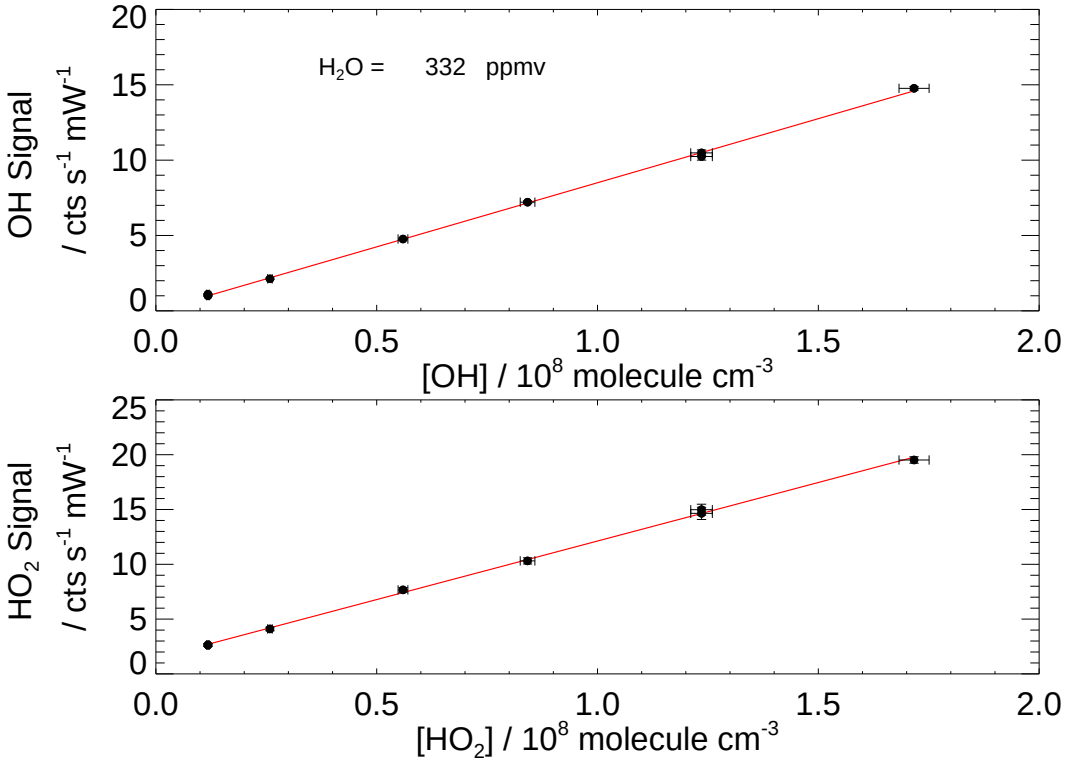

Fig. 5. Multipoint calibration for OH and HO_2 at a constant water vapour (332 ppmv). Calibrations were conducted for a range of water vapour mixing ratios between 10 000 ppmv and 332 ppmv. The lamp current was varied to produce a range of OH and HO_2 concentrations from 1×10^7 to 1.7×10^8 molecule cm^3. Error bars indicate the standard deviation of the data within each data point.

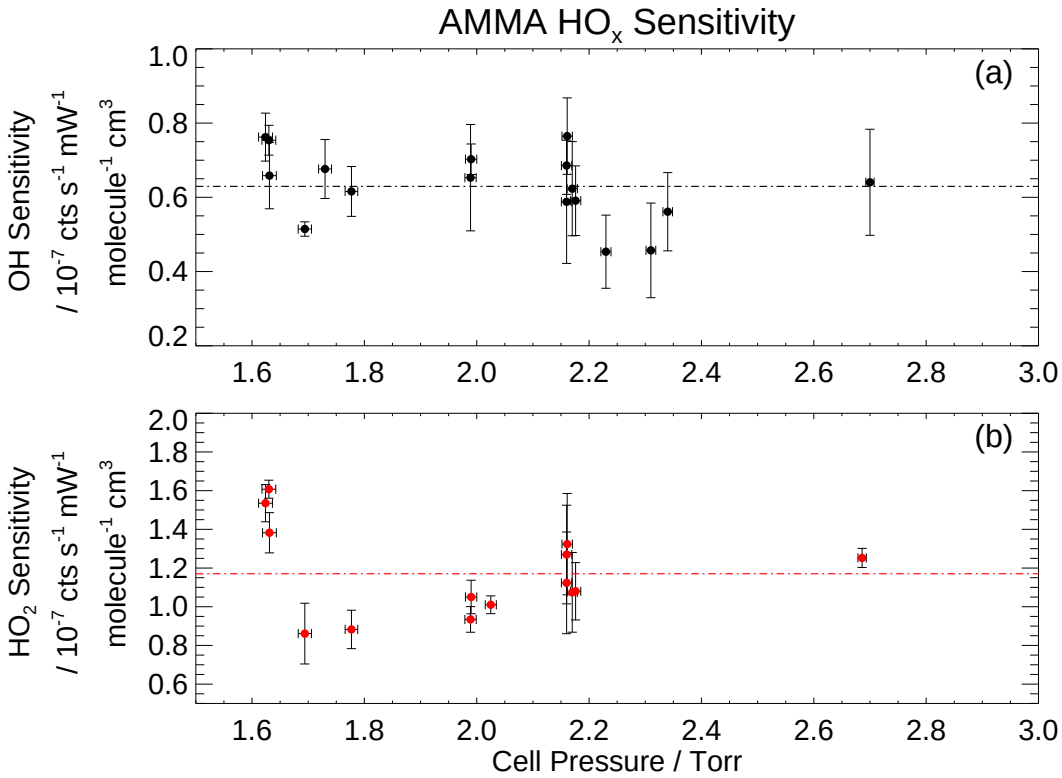

Fig. 6. Instrument Sensitivity as a function of fluorescence cell pressure for OH **(a)** and HO_2 **(b)**. During AMMA, the cell pressure varied between 1.5 Torr (9 km altitude) and 2.1 Torr (sea level). The dashed line indicates the mean sensitivity used for the AMMA dataset.

ACPD
10, 7265–7322, 2010

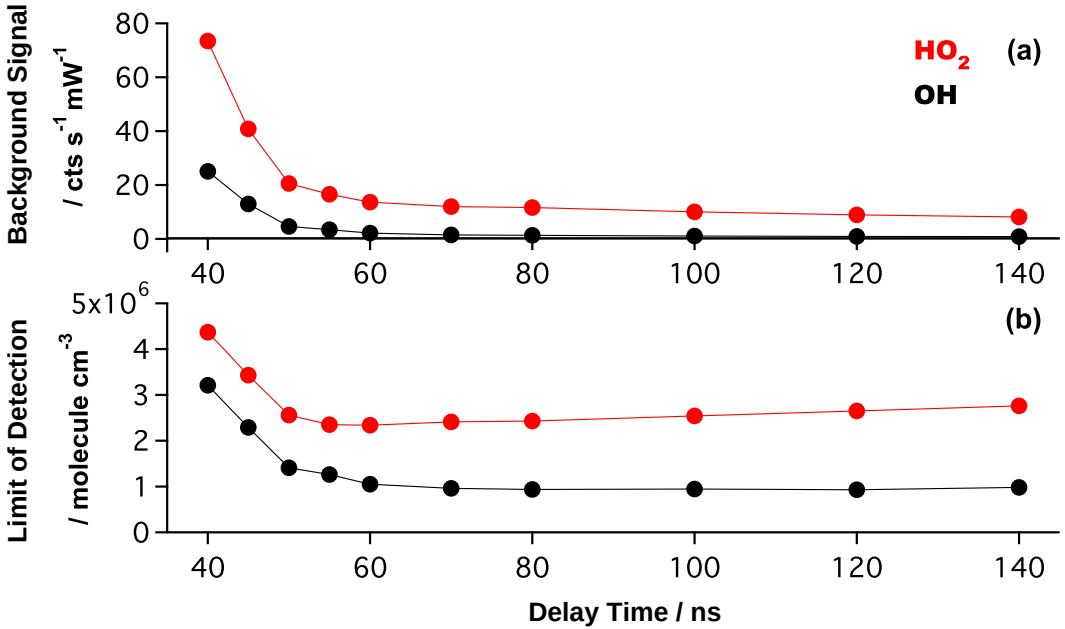

Fig. 7. Typical instrument performance for OH (Black) and HO_2 (Red) changes with the time interval between laser trigger and fluorescence collection. **(a)** Background signal (cts s^{-1} mW^{-1}) and **(b)** Limit of Detection (molecule cm^{-3}).

ACPD
10, 7265–7322, 2010

Title Page
Abstract Introduction
Conclusions References
Tables Figures
◀I ▶I
◀ ▶
Back Close
Full Screen / Esc
Printer-friendly Version
Interactive Discussion

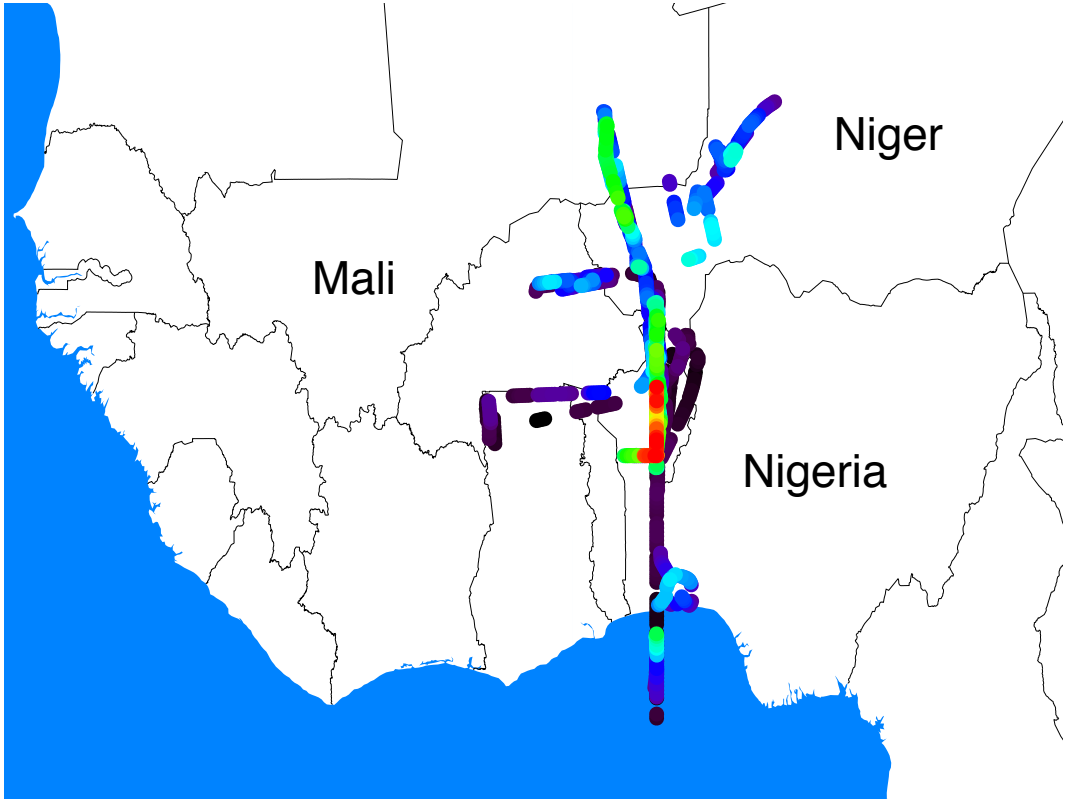

Fig. 8. Spatial distribution of HO_2 observed over West Africa during the African Monsoon Multidisciplinary Analyses (AMMA) campaign. Redder colours indicate the highest concentrations of HO_2, which were observed over the forested regions of Benin.

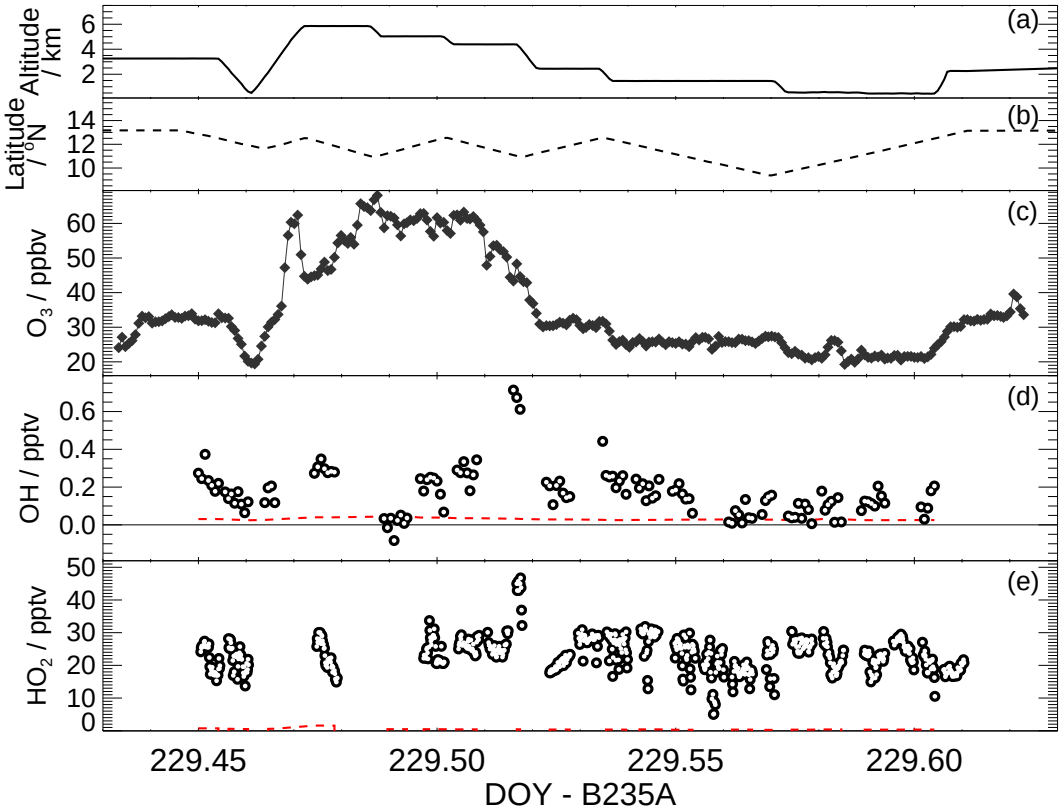

Fig. 9. Time Series of an afternoon flight from 10:40 to 15:00 UTC over the forest region in the north of Benin showing **(a)** altitude (km), **(b)** latitude (° N), **(c)** O_3 (ppbv, blue), **(d)** OH (pptv, black, 60 s resolution) and limit of detection (pptv, red dashed line, 60 s resolution) and **(e)** HO_2 (pptv, black, 10 s resolution) and limit of detection (pptv, red dashed line, 10 s resolution).

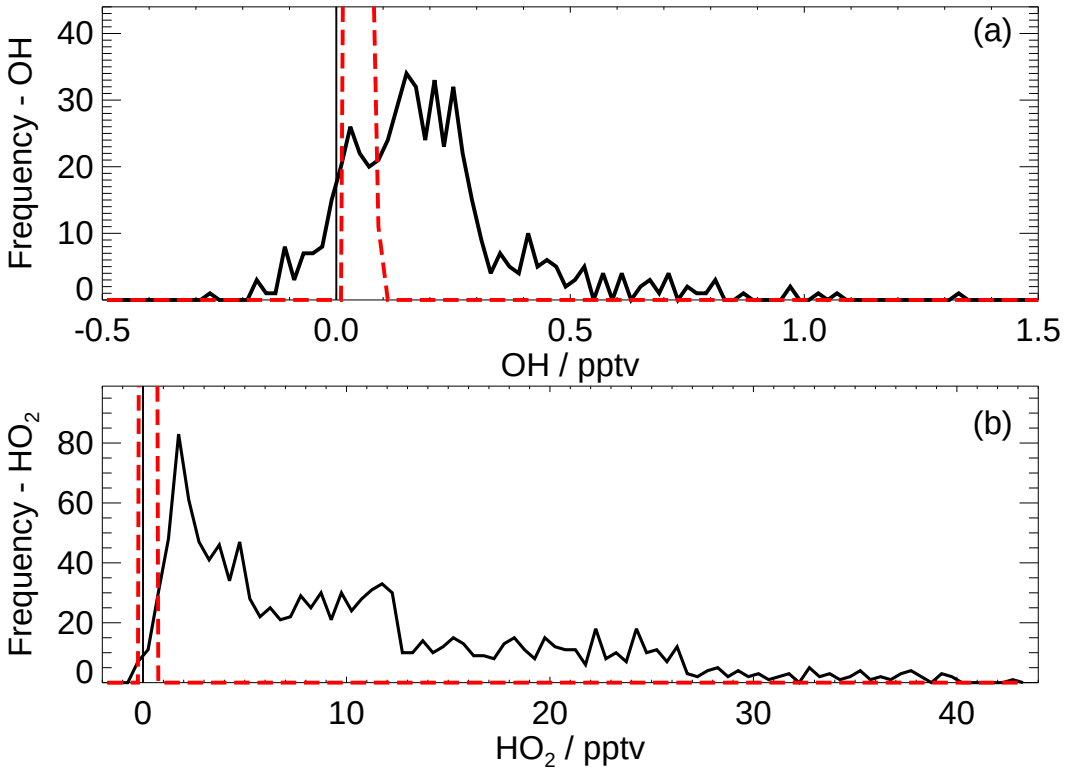

Fig. 10. Probability Density Function (PDF) of observations (solid black lines): **(a)** OH, bin size of 0.02 pptv **(b)** HO_2, bin size of 0.5 pptv. PDF of limits of detection (red dashed lines).

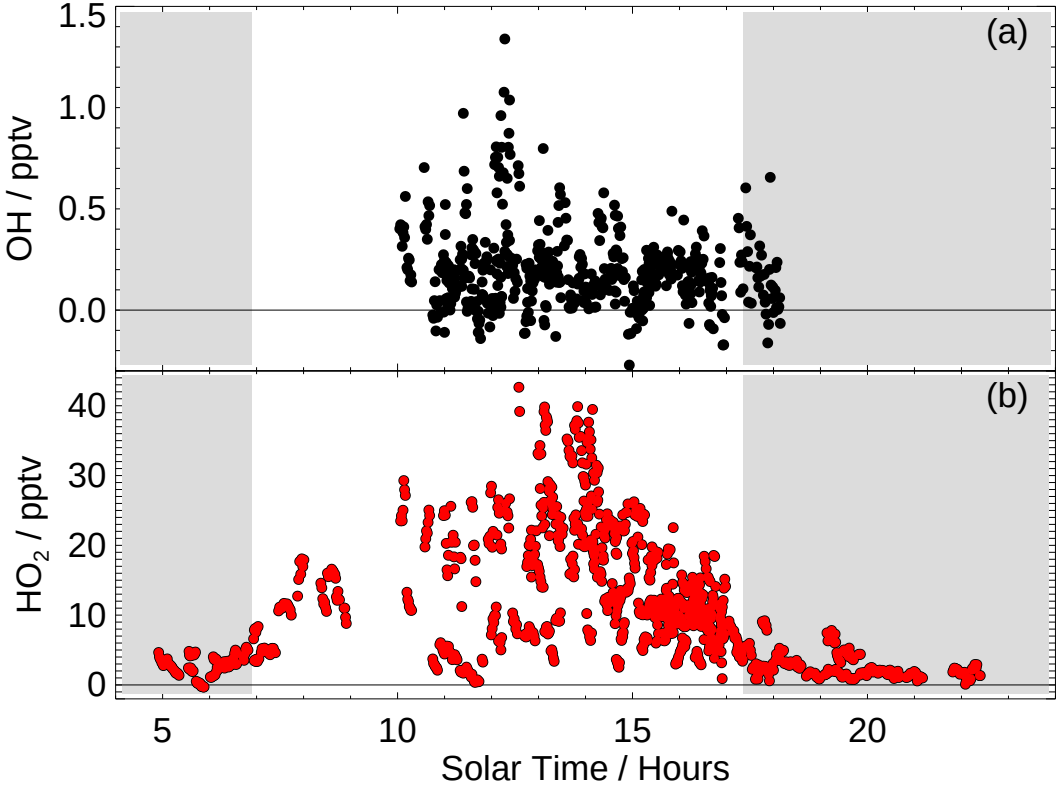

Fig. 11. Diurnal variation of **(a)** OH (pptv) and **(b)** HO_2 (pptv). Shaded areas indicate night.

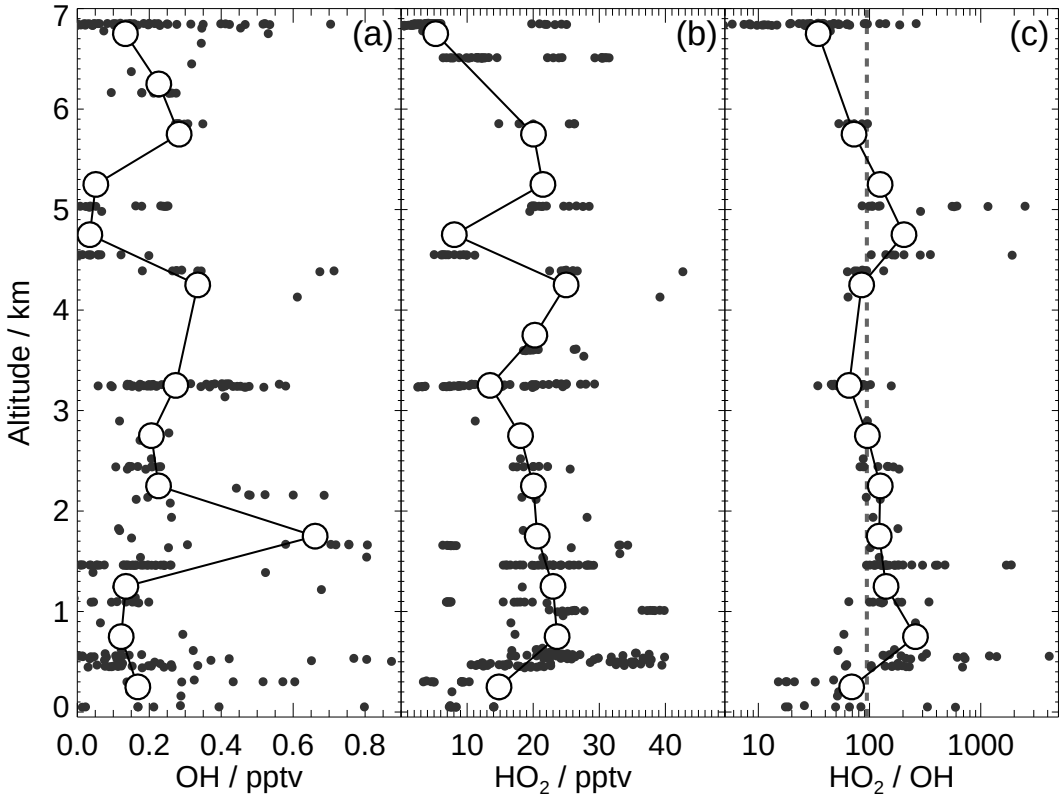

Fig. 12. Median altitude profile of **(a)** OH (pptv, black), **(b)** HO_2 (pptv, black) and **(c)** HO_2/OH ratio. Median values in 500 m altitude bins shown as large joined circles. 60 s data shown as small black dots. Data between 09:00 and 15:00 UTC. The median HO_2/OH ratio of 95 is shown as a grey dashed line.

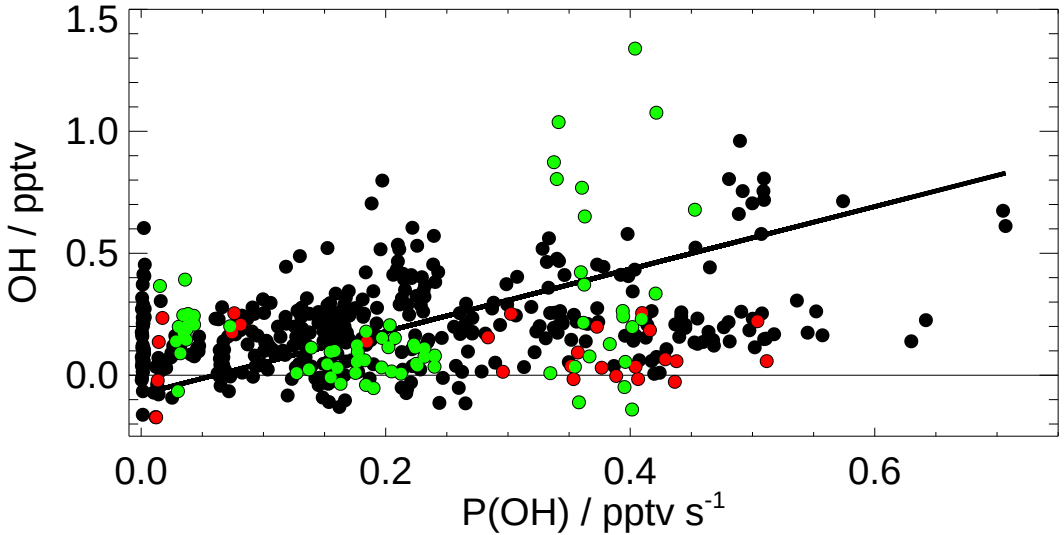

Fig. 13. Correlation between OH (pptv) and P(OH) (pptv s^{-1}): slope =1.28 s; intercept =−0.1; R=0.32. Green points indicate observations in the boundary layer with isoprene greater than 300 pptv. Red points indicate observations within a biomass burning plume with acetonitrile higher than 250 pptv.

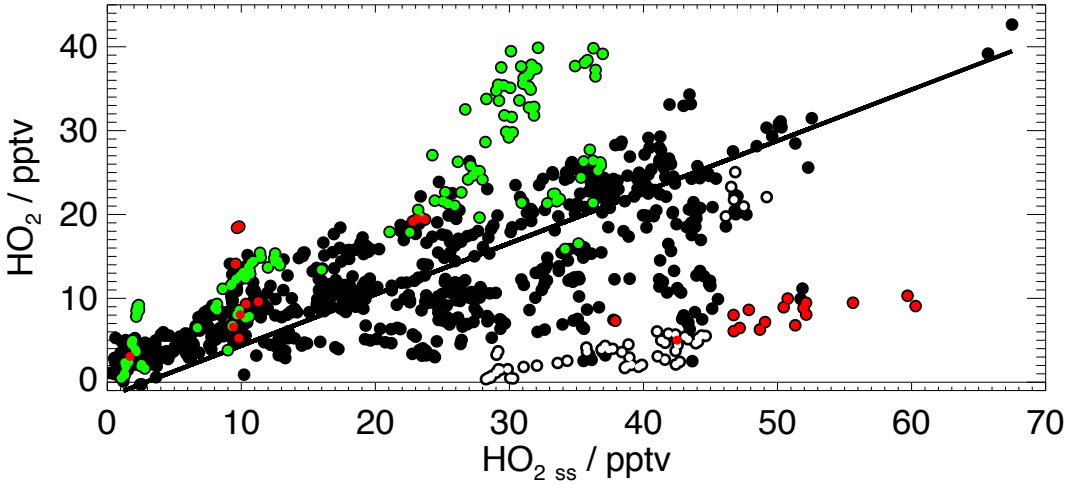

Fig. 14. Correlation between HO_2 (pptv) and $HO_{2\ ss}$ (pptv): slope =0.61; intercept =−1.75; R=0.57. Green points indicate observations in the boundary layer with isoprene greater than 300 pptv. Red points indicate observations within a biomass burning plume with acetonitrile higher than 250 pptv. Open circles indicate observations during Flight 228, when $J(O^1D)$ was significantly greater than expected. Each case is discussed in the text.

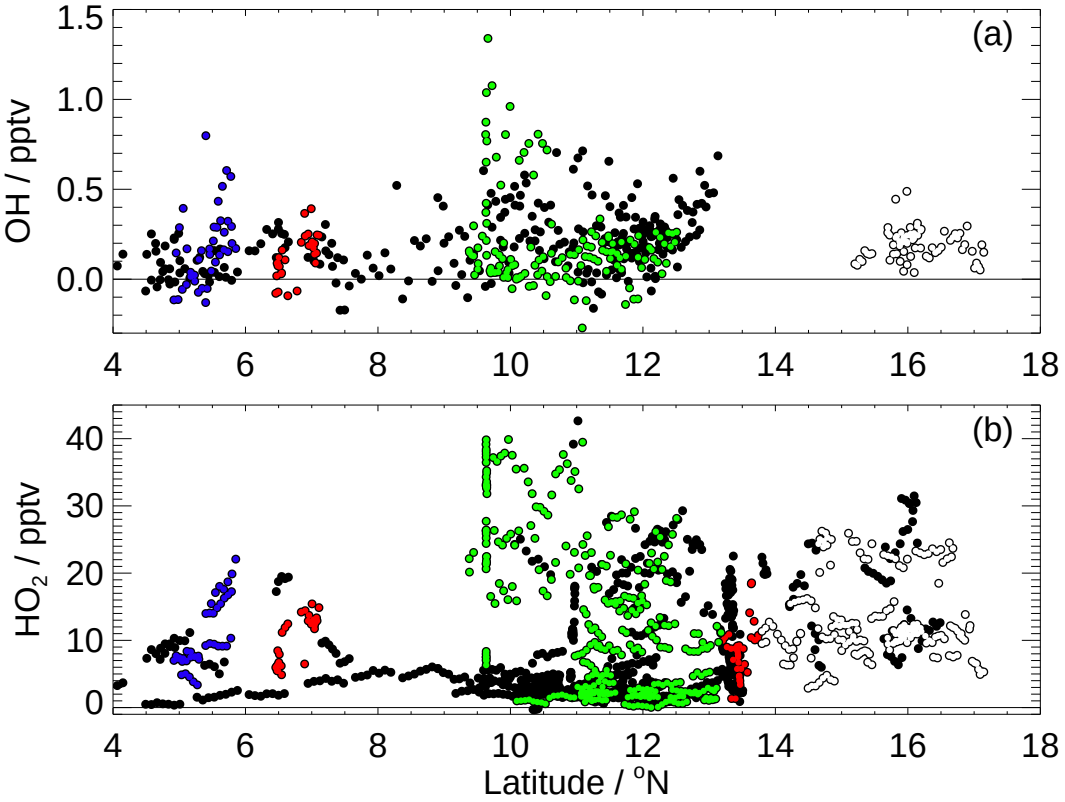

Fig. 15. Latitudinal variation of **(a)** OH and **(b)** HO_2 mixing ratio. Observations in the boundary layer are shown for data collected above the Sahel (13.75–18° N, white), Forest (7.3–13.2° N, green), Ocean (4–6° N, blue) and Urban areas (6–7.3° N and 13.2–13.75° N, red). Observations in the free troposphere in all regions are shown in black.

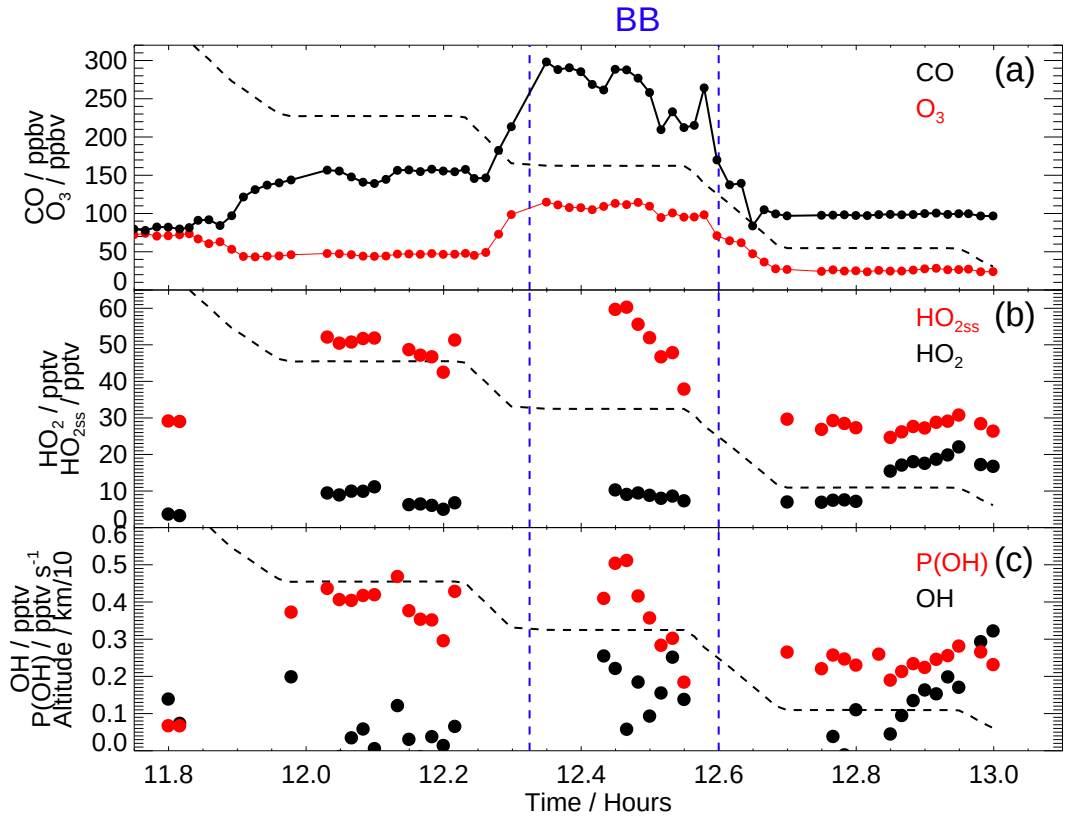

Fig. 16. Time series within and around a Biomass Burning Plume with **(a)** CO (ppbv, black), and O_3 (ppbv, red), **(b)** HO_2 (pptv, black) and $HO_{2\ ss}$ (pptv, red), **(c)** OH (pptv, black) and P(OH) (pptv s^{-1}, red). On all graphs altitude is indicated by a dashed line. 60 s observations.

ACPD
10, 7265–7322, 2010

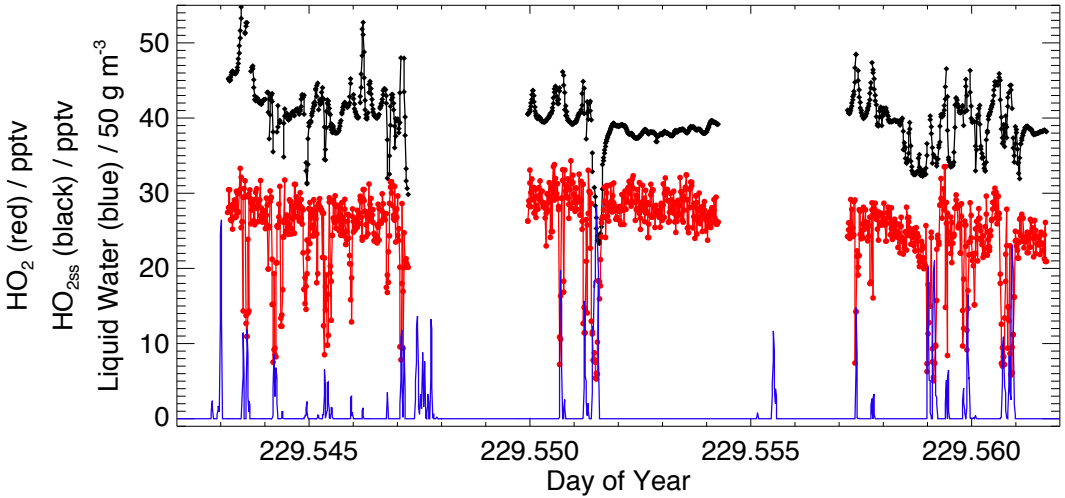

Fig. 17. Time Series of HO_2 variation in Cloud. HO_2 (1 s, pptv, red), $HO_{2\ ss}$ (1 s, pptv, black), Nevzorov probe liquid water content (50 g m^{-3}) (blue). Data was taken between 13:00 and 13:30 UTC at a constant altitude of 1.5 km over northern Benin (10.9—12.5° N).

ACPD
10, 7265–7322, 2010

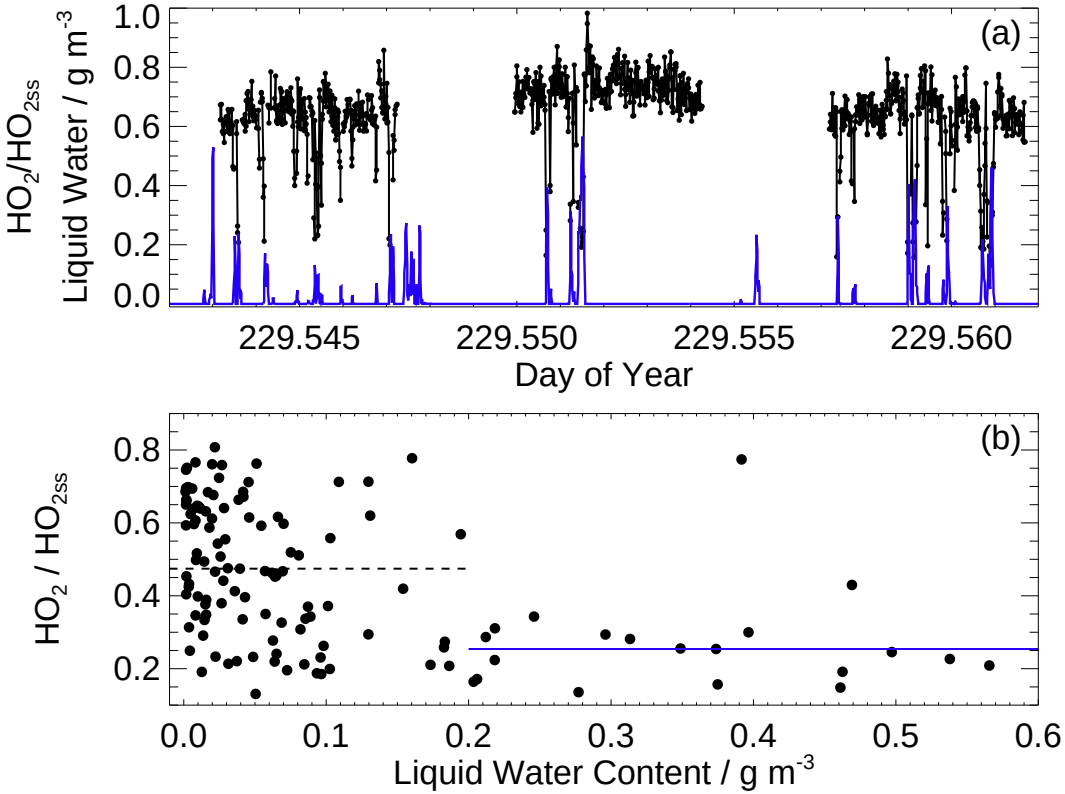

Fig. 18. **(a)** Time Series of $HO_2/HO_{2\,ss}$ ratio (black) and liquid water (blue); **(b)** $HO_2/HO_{2\,ss}$ ratio as a function of liquid water ($g\,m^{-3}$). The median $HO_2/HO_{2\,ss}$ ratio is 0.4 and is shown as a dashed line.

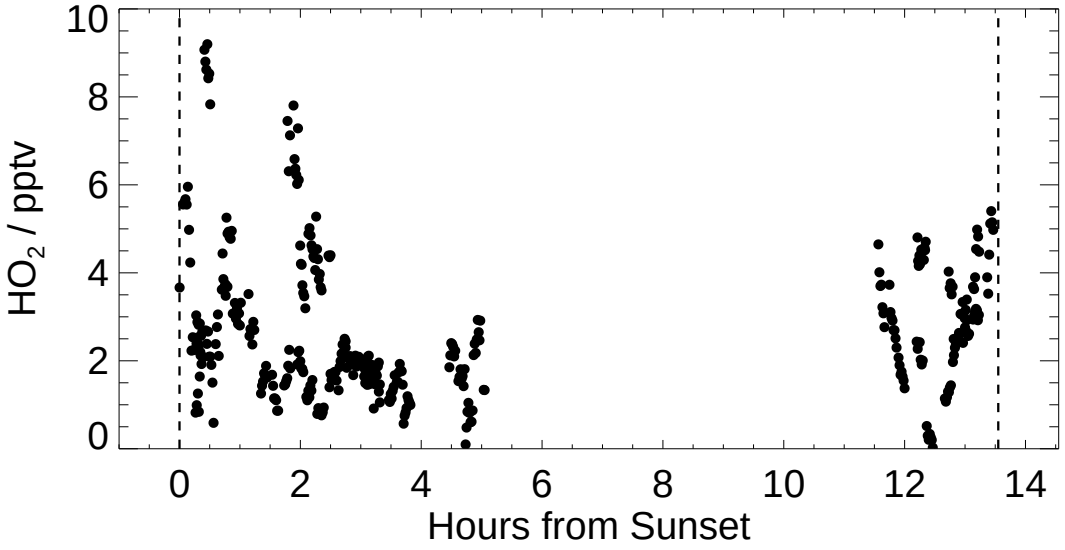

Fig. 19. HO_2 time series as a function of time from sunset. Dawn and dusk are indicated by dashed lines.

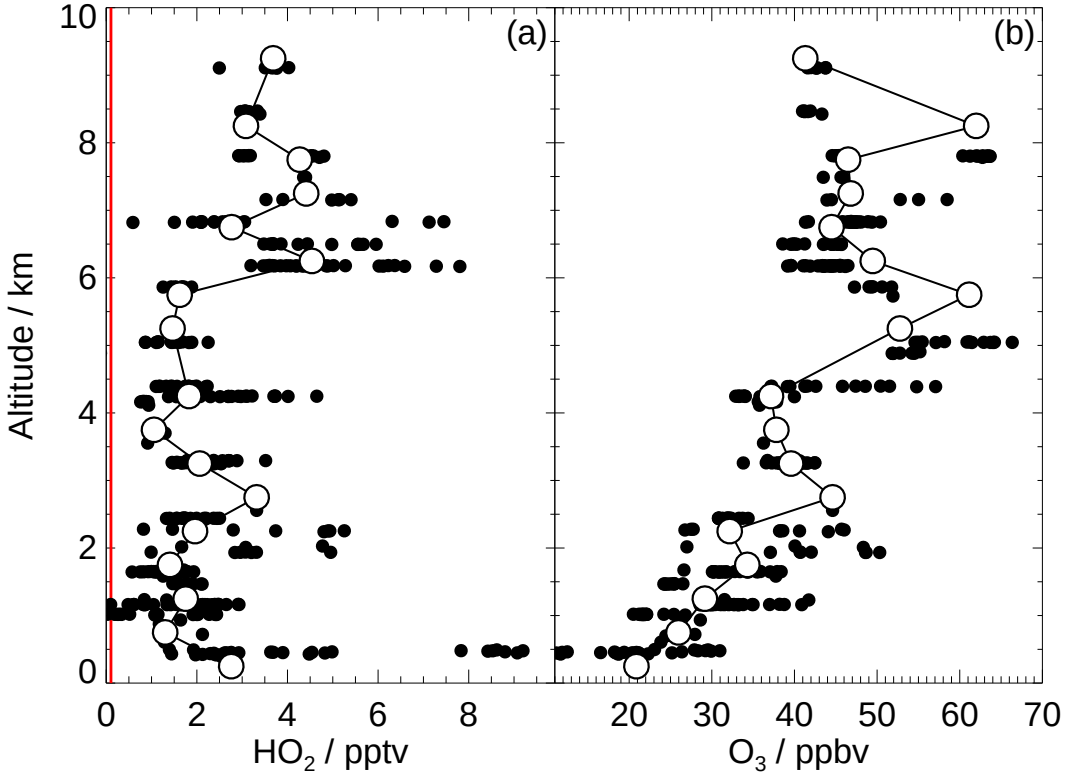

Fig. 20. Night-time Altitude Profiles of **(a)** HO_2 (pptv, black) and maximum HO_2 limit of detection (pptv, red) for the night-time dataset. **(b)** O_3 (ppbv). Median values for 500 m altitude bins are shown as white circles.